A Secondary Zone of Uplift Due to Megathrust Earthquakes

YLONA VAN DINTHER,[1,2] 🄳 LUKAS E. PREISWERK,[1,3,4] and TARAS V. GERYA[4]

Abstract—The 1960 M9.5 Valdivia and 1964 M9.2 Alaska earthquakes caused a decimeters high secondary zone of uplift a few hundred kilometers landward of the trench. We analyze GPS data from the 2010 M8.8 Maule and 2011 M9.0 Tohoku-Oki earthquakes to reveal the persistent existence of a secondary zone of uplift due to great earthquakes at the megathrust interface. This uplift varies in magnitude and location, but consistently occurs at a few hundred kilometers landward from the trench and is likely mainly coseismic in nature. This secondary zone of uplift is systematically predicted by our 2D visco-elasto-plastic seismo-thermo-mechanical numerical simulations, which model both geodynamic and seismic cycle timescales. Through testing hypotheses in both simple and realistic setups, we propose that a superposition of two physical mechanisms could be responsible for this phenomenon. First, a wavelength is introduced through elastic buckling of a visco-elastically layered fore-arc that is horizontally compressed in the interseismic period. The consequent secondary zone of interseismic subsidence is elastically rebound during the earthquake into a secondary zone of relative uplift. Second, absolute and broader uplift is ensured through a mass conservation-driven return flow following accelerated slab penetration due to the megathrust earthquake. The dip and width of the seismogenic zone and resulting (deep) coseismic slip seem to have the largest affect on location and amplitude of the secondary zone of uplift. These results imply that subduction and mantle flow do not occur at constant rates, but are rather modulated by earthquakes. This suggests a link between deep mantle and shallow surface displacements even at time scales of minutes.

Key words: Subduction zone processes, earthquakes, numerical modeling, crustal deformation, geodesy.

[1] Seismology and Wave Physics, Institute of Geophysics, ETH Zürich, Zurich, Switzerland. E-mail: y.vandinther@uu.nl
[2] Department of Earth Sciences, Utrecht University, Utrecht, The Netherlands.
[3] Laboratory of Hydraulics, Hydrology and Glaciology (VAW), ETH Zürich, Zurich, Switzerland.
[4] Geophysical Fluid Dynamics, Institute of Geophysics, ETH Zürich, Zurich, Switzerland.

1. Introduction

The first-order interseismic and coseismic surface displacements of the overriding plate in subduction zones are reasonably well understood (e.g., Wang 2007; Govers et al. 2018). In the interseismic period the overriding plate is coupled to the subducting plate along the seismogenic zone. Subduction thus drags the overriding plate down and landward. This causes subsidence from the trench throughout a large part of the seismogenic zone and interseismic compression causes uplift beyond. This uplift slowly tappers to zero in the far field. In the coseismic period surface displacements typically show elastic rebound of these interseismically accumulated displacements (e.g., Reid 1910; Moreno et al. 2010). This leads to strong uplift of the wedge as the overriding plate slips seaward, while the coastal regions typically located above the hypocenter manifest subsidence. Again farther land inward, standard (visco-)elastic models models show zero vertical displacements (e.g., Wang 2007; Meltzner et al. 2006).

This classical conceptual model is contrasted by two great megathrust earthquakes (i.e., $M_w > 8.5$) in the 1960s in Chile and Alaska, where a distinct secondary zone of uplift was measured landward of the hypocenter (Plafker 1969; Plafker and Savage 1970). However, these static measurements were made long ago and many years after the earthquakes, such that seperating coseismic and early postseismic contributions was not possible. Up to now a secondary zone of uplift is thus not considered as a persistent feature. The classical interpretation of a very gradual tapering to zero uplift is also contrasted by more recent seismo-thermo-mechanical (STM) models, which predict the presence of a secondary zone of uplift (van Dinther et al. 2013b). These models self-consistently simulate both subduction dynamics and

seismogenesis in a setup where visco-elastic structure is governed by conservation laws and a visco-elasto-plastic rheology based on laboratory experiments.

Following the two great megathrust earthquakes in the 1960s several papers identified specific settings and physical mechanisms that would allow for a secondary zone of uplift. For the 1960 M9.5 Valdivia earthquake, Plafker and Savage (1970) reproduced the secondary zone of uplift by introducing a downward curving fault that steepens suddenly. Linde and Silver (1989) reanalyzed the same dataset and suggested that slip must have also occurred until depths up to 65–80 km, while a strong kink in the interface was required below the peak of the secondary bulge to reproduce this feature. Vita-Finzi and Mann (1994) explained the deformation pattern in Valdivia by elastic flexure of a continuous elastic beam following displacements of mass and resulting buoyancy effects. For the 1964 M9.2 Alaska earthquake, Plafker (1969) speculated that it could be caused by a sudden increase in horizontal compressional strain and termed it a 'Poisson bulge', while noting this feature as a major unresolved problem. Alternatively, Plafker (1972) shortly postulated a hypothesis of transverse crustal buckling resulting from horizontal compression of the continental plate.

The occurrence of great megathrust earthquakes in the last decade allowed for major advances in understanding surface displacements (e.g., Kido et al. 2011; Fujiwara et al. 2011; Wang et al. 2012; Sun et al. 2014; Klein et al. 2016; Govers et al. 2018). However, models aiming to reproduce the displacements during the 2010 and 2011 megathrust earthquakes do typically not reproduce a secondary zone of uplift (e.g., Govers et al. 2018). Interestingly some models do reproduce a similar uplift, but secondary zones of uplift are not described as such (Miyashita 1987) or are produced by postseismic mechanisms only (Klein et al. 2016; Li et al. 2017).

This literature overview shows that there is no consensus on whether a secondary zone of uplift is a universal physical phenomenon. Additionally, there is no consensus on the physical mechanisms responsible for such a secondary zone of uplift. Through re-analyzing high-quality data from the last decade and dedicated numerical models (Sect. 2) we aim to understand whether the classical conceptual model of surface displacements should be extended with a secondary zone of uplift. Our analysis of published data for four great megathrust earthquakes confirms the existence of a secondary zone of uplift (Sect. 3.1). We then study STM models of different degrees of complexity to propose two physical mechanisms working together to form a secondary zone of uplift (Sects. 3.2–3.4). Finally, we discuss the limitations, implications and predictions of our findings (Sect. 4).

2. Methods

2.1. Data Collection from Literature

A secondary zone of uplift in nature can be detected by surveying land elevations before and after an earthquake. Decades ago methods as described in e.g. Plafker (1965) and Plafker and Savage (1970) provided estimates with measurement uncertainties on the order of a few decimeters. Near the coast line relative sea level changes were mapped using local markers, such as high-tide lines or vertical growth limits up to which specific sessile marine organisms or plants can live. Inland elevation changes were obtained by differencing results from leveling methods obtained in two subsequent surveys. Nowadays, land-based GPS data provide widespread information on vertical displacements with an accuracy on the order of centimeters.

We analyze the megathrust earthquakes for which a decent amount of measurements exists at a few hundred kilometers landward from the trench. This requires a coastline for relative sea level change measurements or land for GPS measurements. Accordingly, we identified four megathrust earthquakes: the 1960 M9.5 Valdivia (Plafker and Savage 1970), 1964 M9.2 Alaska (Plafker 1969), 2010 M8.8 Maule (Vigny et al. 2011) and 2011 M9.0 Tohoku-Oki (Ozawa et al. 2011; Sato et al. 2011) earthquakes. For these earthquakes, we combined published data into trench-perpendicular profiles of vertical displacements. Relevant aspects regarding the origin of these datasets, specific values for the resulting secondary zone of uplift, and the corresponding tectonic parameters for each subduction zone are summarized in Table 1. The values and uncertainties in the data are adopted from the

Table 1

An overview of the differences between studied earthquakes and data acquisition methods. Data sources: [a]*Plafker and Savage (1970),* [b]*Plafker (1969),* [c]*Vigny et al. (2011),* [d]*Ozawa et al. (2011),* [e]*Sato et al. (2011),* [f]*Johnson et al. (1996),* [g]*Holdahl and Sauber (1994),* [h]*Yue and Lay (2013),* [i]*Moreno et al. (2009),* [j]*Holdahl and Sauber (1994),* [k]*Moreno et al. (2014),* [l]*Hayes et al. (2012),* [m]*Heuret et al. (2011)*

	1960 M9.5 Valdivia	1964 M9.2 Alaska	2010 M8.8 Maule	2011 M9.0 Tohoku-Oki
Data type	Growth limits, eyewitness accounts[a]	Growth limits, leveling survey[b]	GPS[c]	GPS[d], seafloor geodesy[e]
Time span between earthquake and survey (Δt)	8 years	1–2 years	2–20 days	4 h (GPS), 1–4 months (sea floor geodesy)
Uncertainty	20–100 cm	30 cm	1–10 cm	2 cm (GPS), 20–60 cm (geodesy)
Peak slip	20–40 m[a]	22–30 m[f,g]	15 m[c]	50–60 m[h]
Rupture width	$\sim$ 130 km[i]	$\sim$ 300 km[j]	$\sim$ 190 km[k]	$\sim$ 200 km[d]
Average interface dip	21°[l]	12°[l]	21°[l]	17°[l]
Seismogenic zone downdip limit	210 km[m]	243 km[m]	135 km[m]	210 km[m]
First hinge point (HP_1)	95 km	215 km	120 km	120 km
Second hinge point (HP_2)	200 km	350 km (E), 500 km (W)	240 km	335 km
Primary subsidence ($S_{1,max}$)	2.7 m	1.9 m	0.73 m	1.158 m
Secondary uplift ($U_{2,max}$)	1.1 m	0.3 m	0.12 m	0.04 m

The time span between earthquake and survey (Δt) provides an indication of the potential amount of postseismic data included, while the uncertainties amongst others depend on the measuring techniques. We include estimates of peak slip, rupture width (defined as downdip width of the zone with slip > 5 m), average interface dip (defined here as the average dip for 100 km depth), and downdip limit of the seismogenic zone from the literature. The lowermost block characterizes the surface displacements: HP_1 is the transition from primary uplift to subsidence (first hinge point), whereas HP_2 is the second hinge point (the transition from subsidence to secondary uplift). $S_{1,max}$ is the maximum subsidence of the primary zone of subsidence and $U_{2,max}$ denotes maximum uplift of the secondary zone of uplift

referenced studies (Plafker and Savage 1970; Plafker 1969; Vigny et al. 2011; Ozawa et al. 2011; Sato et al. 2011). In general, uncertainties decrease as measurements are done later in time with more accurate acquisition methods. Furthermore, the time interval between the earthquake and survey (Δt) gives a rough indication for the amount of postseismic deformation that is potentially included in the displacement data (see discussion in Sect. 4.3).

2.2. Numerical Model

We use the seismo-thermo-mechanical (STM) numerical models developed and detailed in van Dinther et al. (2013a), van Dinther et al. (2013b), and van Dinther et al. (2014). These models are based on the continuum-mechanics framework of I2ELVIS, which is a 2-D implicit, conservative finite difference thermo-mechanical code (Gerya and Yuen 2007). The fully staggered Eulerian grid is combined with a Lagrangian marker-in-cell technique to allow for large deformation through advecting properties (e.g. lithology, material parameters and stress) along with

the particles they belong to. The code solves for the pressure as well as horizontal and vertical velocity assuming conservation of mass in an incompressible medium (Eq. 5) and conservation of momentum with gravity and inertia (see Appendix 1, Eqs. 6, 7). The large-scale models also solve for temperature using the heat equation including advection, conduction, and heat generation due to shear heating, radioactive heating and adiabatic (de-)compression (Appendix 1, Eq. 8). Additionally, the large-scale setup includes basic formulations of (de-)hydration, fluid flow, and erosion (van Dinther et al. 2013b).

The constitutive equations relate strain rates $\dot{\varepsilon}'_{ij}$ to deviatoric stresses σ'_{ij} using a non-linear visco-elasto-plastic rheology according to

$$\dot{\varepsilon}'_{ij} = \underbrace{\frac{1}{2\eta} \cdot \sigma'_{ij}}_{\dot{\varepsilon}'_{ij(viscous)}} + \underbrace{\frac{1}{2G} \cdot \frac{D\sigma'_{ij}}{Dt}}_{\dot{\varepsilon}'_{ij(elastic)}} + \underbrace{\begin{cases} 0 & \text{for } \sigma'_{II} < \sigma_{yield} \\ \chi \frac{\partial g_{plastic}}{\partial \sigma'_{ij}} & \text{for } \sigma'_{II} = \sigma_{yield} \end{cases}}_{\dot{\varepsilon}'_{ij(plastic)}}.$$

(1)

This represents a Maxwell visco-elastic body in series with a frictional plastic slider, where η is effective

viscosity, G is shear modulus, $\frac{D\sigma'_{ij}}{Dt}$ is the objective co-rotational time derivative solved using a time explicit scheme, $g_{plastic}$ is the plastic flow potential, χ is the plastic multiplier connecting plastic strain rates and stresses, and σ_{yield} is the plastic yield strength. The amount of elastic versus viscous deformation is determined by the viscoelasticity factor $(G\Delta t)/(G\Delta t + \eta_{vp})$ (e.g., Moresi et al. 2003; Gerya 2010). The non-linear ductile viscosity η is based on experimentally derived dislocation creep flow laws as

$$\eta = \left(\frac{1}{\sigma'_{II}}\right)^{(n-1)} \cdot \frac{1}{2A_D} \cdot \exp\left(\frac{E_a + PV_a}{RT}\right), \quad (2)$$

where R is the gas constant (8.314 J/(mol °C). Stress exponent n, pre-exponential factor A_D, activation energy E_a and activation volume V_a are experimentally determined parameters set for each lithology.

Brittle deformation is modeled using non-associative plasticity with a pore fluid pressure-effective pressure-dependent yield strength

$$\sigma_{yield} = C + \mu \cdot \left(1 - \frac{P_f}{P_s}\right) \cdot P. \quad (3)$$

Earthquake-like events result from a strongly slip rate-dependent frictional formulation with

$$\mu_{eff} = \mu_s(1 - \gamma) + \mu_s \frac{\gamma}{1 + \frac{V}{V_c}}, \quad (4)$$

where μ_s is the static friction coefficient, V_c is the characteristic velocity, and γ represents the amount of slip velocity-induced weakening (i.e., $1 - \frac{\mu_d}{\mu_s}$, where μ_d is the dynamic friction coefficient). Spontaneous ruptures represent the occurrence of rapid threshold-exceeding slip during which permanent displacement and stress drop occur along a localized interface (van Dinther et al. 2013b).

In summary, the resulting code handles both long-term subduction dynamics and short-term seismogenesis in a physically consistent manner. In the large-scale setup this means that the slab and seismogenic zone geometries together with its thermal and viscosity structures evolve autonomously. They influence the corresponding stress and strength distributions, which ultimately lead to the generation of spontaneous earthquake-akin events. Hence we model the interaction between the lithosphere, slab and mantle through spontaneously developing faults

and events. An important disadvantage of the current version is that events durations are very long (on the order of a $\sim$ 100 years) due to the constant time step of 5 years (van Dinther et al. 2013b). This makes inertial dynamics negligible and prevents us from uniquely distinguishing coseismic from postseismic processes. However, inertial dynamics in terms of shear wave propagation is resolved in the simplified analogue model setup, although waves are somewhat slow due to low scaled shear wave speeds of gelatin.

2.3. Model Setups

To better narrow down the physical mechanisms governing a secondary zone of uplift we use two model setups. These setups vary in degree of lithological, rheological and geometrical complexity.

The most realistic setup represents a 1500 × 400 km² trench-normal section of the Southern Chilean active continental margin, which is similar albeit deeper than the setup used in van Dinther et al. (2013b) and van Dinther et al. (2014) (Fig. 1a). The setup in the seismic cycle phase spontaneously evolved from about 5 million years of thermo-mechanical subduction of an oceanic slab of age 40 Ma due to a slab push at a steady rate of 7.5 cm/year. This lead to a large sedimentary wedge adjacent to a continental overriding plate beneath which an oceanic crust and lithospheric mantle subduct into a visco-elastic upper mantle. The visco-elasto-plastic parameters of each lithology are based on a range of laboratory experiments and are similar to van Dinther et al. (2014). These parameters within the governing and constitutive equations (Sect. 2.2) lead to a self-consistent thermo-mechanical structure in which viscosity is calculated according a temperature-, pressure-, and stress-dependent flow law dominated by dislocation creep (Eq. 2). The resulting smooth viscosity profile contains a lower continental crust with a viscosity of about 10^{21-22}Pa s and an asthenospheric mantle with a viscosity on the order of 10^{18-20} Pa s (Fig. 1a). The subduction channel is largely formed by the top 2 km of oceanic crust, which accommodates most deformation and spontaneously transits from brittle to ductile deformation between about 350 and 450 °C (van Dinther et al.
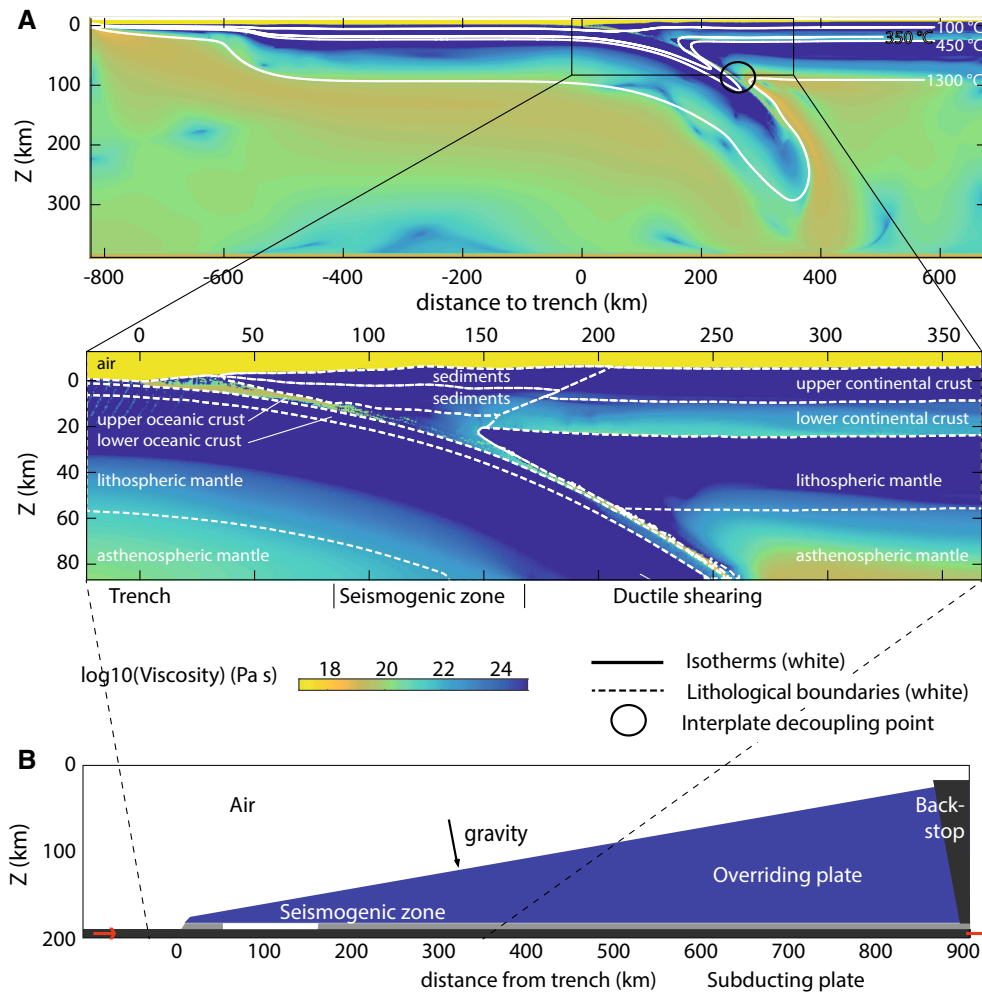
Figure 1

a Model setup of seismo-thermo-mechanical (STM) model with a large-scale setting resembling Southern Chile (van Dinther et al. 2013b). Top shows the entire model with relevant isotherms in white, whereas the lower panel shows a zoom on the region of interest and depicts the rock types and their boundaries in white. **b** Model setup of seismo-mechanical model (van Dinther et al. 2013a) simulating the analogue model of Corbi et al. (2013). Colors in all panels indicate the same viscosity scale

2013b). In terms of frictional parameters this megathrust interface is slip rate weakening ($\mu_s = 0.5$, $\mu_d = 0.15$, $\frac{P_f}{P_s} = 0.95$), but for the shallowest section at which a transition to slip rate strengthening occurs from 150 to 100 °C.

The simplified setup is adapted from van Dinther et al. (2013a) and is based on the upscaled analogue modeling setup of Corbi et al. (2013). In this setup a rigid, straight slab subducts beneath a (visco-)elastic wedge, which is bounded by a rigid backstop (Fig. 1b). For ease of numerical computation we rotate the setup and gravity by a slab dip of 10° to align the megathrust interface and slab with the lower

boundary. The wedge-shaped fore-arc is confined by a backstop, which is moved further away from the trench to reduce its influence on simulated surface displacements to a minimum (see Sect. 3.3.1). The fore-arc wedge deforms elastically (99.7%). In this study we add lower crustal and upper mantle layers that largely deform viscously (98%). The megathrust interface additionally features plastic deformation, as controlled by a seismogenic zone with slip rate weakening friction bounded by slip rate strengthening friction regions.

In each setup a sticky air layer at the top deforms viscously at all time steps and approximates a free

surface (Crameri et al. 2011; van Dinther et al. 2013b). This allows for unhampered evolution of both temporal and permanent topography.

3. Results and Analysis

We first compile published vertical displacement data to understand how universal a secondary zone of uplift is (Sect. 3.1). Second we study the universality, characteristics and evolution of a secondary zone of uplift in seismo-thermo-mechanical models with a realistic setup tailored to Southern Chile (Sect. 3.2). Section 3.3 analyzes the physical mechanisms responsible for such a secondary zone of uplift through studying both a realistic Southern Chile setup and a simplified wedge model. Finally, we discuss some parameters influencing a secondary zone of uplift (Sect. 3.4).

3.1. Natural Data

3.1.1 Coseismic Vertical Displacements

To understand whether a secondary zone of uplift exists in all great megathrust earthquakes we compile the available vertical surface displacements due to great megathrust earthquakes. These displacements aim to capture coseismic displacements, but postseismic displacements are included when a larger time lag since the earthquake is involved (Table 1). The collected data for four out of four great earthquakes show a secondary zone of uplift (Figs. 2, 3). These secondary zones of uplift are remarkably spatially coherent with 164 out of 167 measurements indicating uplift (Fig. 2). Two measurements that show subsidence are obtained near the second hinge point of the 1960 Valdivia earthquake, which is the location where subsidence changes to uplift (HP_2). The location and magnitude of this secondary zone of uplift, however, vary significantly from one tectonic region to another. This can be appreciated quantitatively by studying Table 1), which contains the available data on the secondary zone of uplift and relating earthquake characteristics for each event.
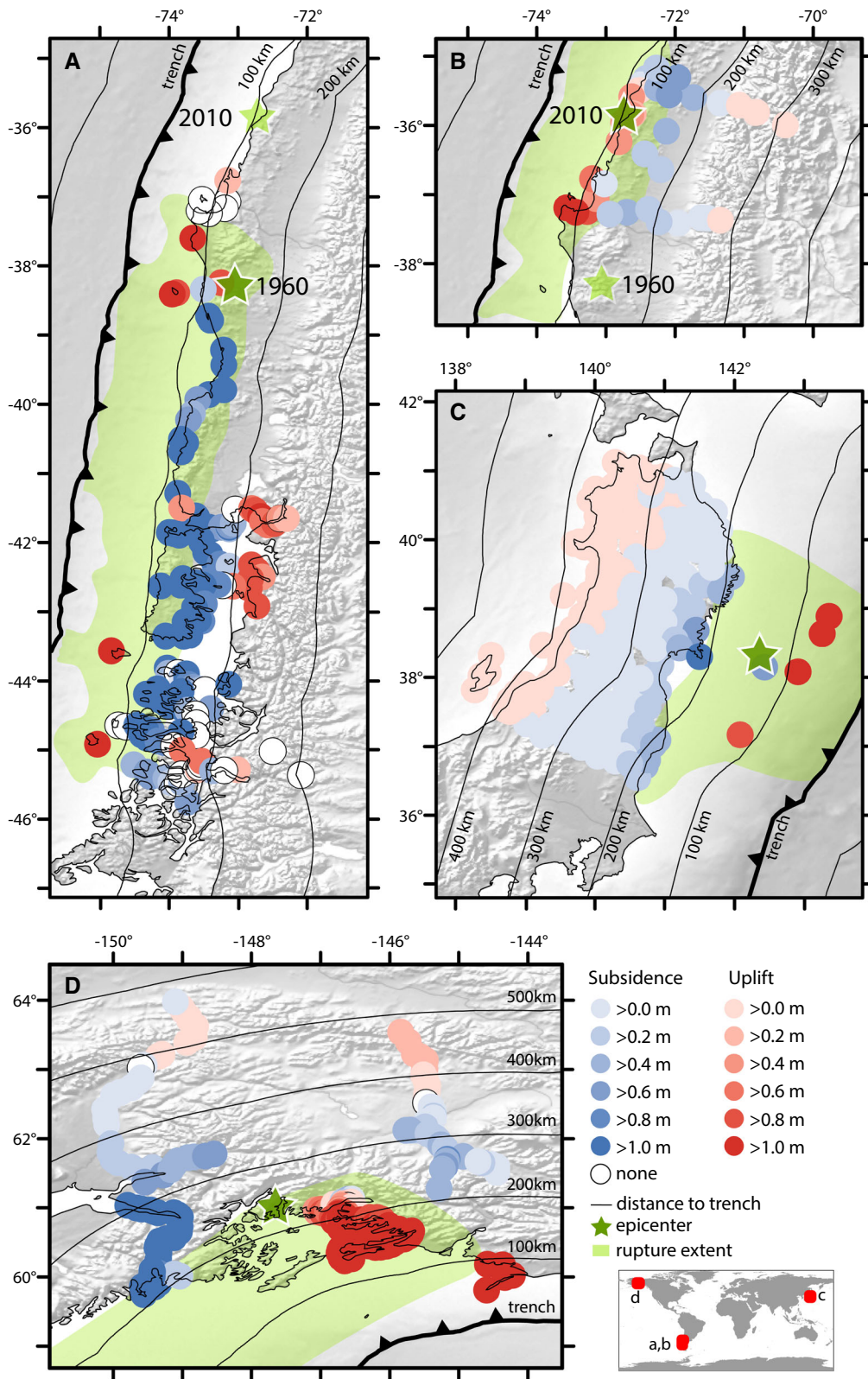
Figure 2 ▶

Map view of the surface displacements in **a** southern Chile due to the M9.5 Valdivia earthquake, **b** central Chile due to the 2010 M8.8 Maule earthquake, **c** north-east Japan due to the 2011 M9.0 Tohoku-Oki earthquake, and **d** Alaska due to the 1964 M9.2 Alaska earthquake. Uplift is red, while subsidence is blue. Displacements aim to represent coseismic displacements, but due to a time lag in measurements various amounts of postseismic displacements can be included (see "time span" row in Table 1, where time lags vary from a few hours to a few years). Sources are given in the "data type" row of Table 1. Green stars denote epicenters and green shaded areas are approximate areas of coseismic slip. Thick black lines are the trenches (Coffin et al. 1998) and thin black lines indicate the horizontal distance to the trench with multiples of a 100 km. In all earthquakes studied, there is a secondary zone of uplift, but the second hinge point is at different distances from the trench

Within the comparable Chilean tectonic region, we observe a correlation in uplift magnitude with earthquake magnitude and slip. The M9.5 Valdivia earthquake shows a distinct secondary zone of uplift with a second hinge point at around 200 km from the trench and a maximum secondary uplift $U_{2,max}$ of ~ 1 m (Fig. 3a). The data points are more scattered due to large measurements errors (in the range of 20–60 cm) as well as local tectonic variations over a wide range during the long period of 8 years between earthquake and survey. The smaller 2010 M8.8 Maule earthquake ruptured the same subduction zone just north of the Valdivia earthquake. This earthquake also showed a secondary uplift with roughly 10 times smaller amplitude $U_{2,max}$ at roughly 50 km farther from the trench (HP_2 at 240 km, Fig. 3b).

The M9.0 Tohoku-Oki earthquake produced a minor secondary zone of uplift with uplift of about 4 cm beyond about 335 km from the trench (Fig. 3c). The map view confirms this minor uplift is widespread and spatially coherent uplift with all 64 stations landward of the main slip area measuring it (Fig. 2c).

The M9.2 Alaska earthquake caused a secondary uplift $U_{2,max}$ of maximum 0.3 m with a contrast between the eastern profile (recorded along the Richardson Highway) and the western profile (Alaska railroad, Fig. 3d). The second hinge point at the western transect was measured at ~ 500 km, while it occurred at ~ 350 km for the eastern transect (Fig. 2d). This difference could arise from the location with respect to the lateral limit of the rupture

or from the sharp bend of the slab and trench in Alaska, which influences the slab dip. Such large differences in location of the secondary zone of uplift within one earthquake are not observed for the Chilean and Tohoku earthquakes, where the trenches and slabs are rather straight.

From the 2004 M9.2 Sumatra-Andaman earthquake, GPS stations in our region of interest that recorded the earthquake are limited to two stations (see Figs. 1b, 2n, o; Table 2 in Hashimoto et al. 2006). Station SAMP at the eastern side of Sumatra is located at roughly 400 km from the trench and recorded an uplift of 6.2 ± 8.5 mm. Additionally, an uplift of 12.5 ± 7.3 mm was recorded at 600–700 km from the trench in Phuket (Thailand). Interestingly, levelling data following the 1946 M8.2 Nankaido earthquake also shows three out of three locations with uplift in a secondary zone beyond 250 km from the trench (see Fig. 10 in Miyashita 1987). These two and three uplift measurements suggest a secondary zone of uplift could also be present for the 2004 M9.2 Sumatra-Andaman and 1946 M8.2 Nankaido earthquakes. Nonetheless, due the limited statistical meaning of both two and three data points in space, we exclude these two earthquakes from our formal analysis. We did not analyze the limited data in the area of interest for any other $M < 8.5$ earthquake.

3.1.2 Deciphering Tectonic Control

In an attempt to decipher which tectonic features influence this secondary zone of uplift, we compare values for this admittedly too low number of four earthquakes (Table 1). The amount of secondary uplift $U_{2,max}$ seems somewhat correlated to earthquake magnitude and thus the total amount of slip. Total slip can for this be approximated as amount of slip times slip area, which is derived from moment magnitude scaled to seismic moment (Blaser et al. 2010) and assumes shear moduli are roughly equal. More total slip or larger magnitude leads to a higher secondary zone of uplift with the exception of the M9.0 Tohoku earthquake. However, the amount of slip on the shallow portion of the Tohoku megathrust interface was exceptional (e.g., Fujiwara et al. 2011).

The distance from the second hinge point HP_2 to the trench seems to increase with the downdip width of each rupture and decrease with the dip of the megathrust interface (Table 1). Alaska with the flattest subduction zone shows the most horizontally stretched pattern, whereas the Chilean slab dips most steeply and show a more compressed uplift pattern (Figs. 3, 4). This suggests that if earthquake slip penetrates farther away from the trench, the secondary zone of uplift is shifted accordingly.

In summary, all four megathrust earthquakes studied show a similar displacement pattern including a secondary zone of uplift. Differences in amplitude and hinge point position are considerable and are likely related to slab geometry and rupture size.

3.1.3 Postseismic Vertical Displacements

The data targeting coseismic displacements include different amounts of postseismic deformation mainly due to the different delay times when measuring the displacements (Table 1). To better constrain the coseismic or postseismic nature of secondary uplift, we shortly analyze the vertical displacements in the locations that showed a secondary zone of uplift for the 2011 and 2010 earthquakes (Fig. 2).

The stations that showed secondary coseismic uplift in the 2010 M8.8 Maule earthquake still show uplift up to 4 years after the event (e.g., Klein et al. 2016). However, the uplift rates are decreasing significantly. Averaged uplift rates up to 400 cm/year were observed in measurements best approximating the coseismic phase (Vigny et al. 2011). In the postseismic phase this uplift rate reduces to 5 cm/year in month 2–6 and 1.3 cm/year two to three years after (Klein et al. 2016). This significantly slower postseismic uplift corresponds to the mid-field zone of postseismic uplift as observed and potentially explained by Klein et al. (2016) and Li et al. (2017).

These findings of early postseismic uplift in the region of interest are contrasted by early postseismic observations following the 2011 M9.0 Tohoku earthquake. In Japan west coast stations showed coseismic uplift, as observed in the measurements done within 4 h after the earthquake [Figs. 2, 3 showing data from Ozawa et al. (2011)]. However, these west coast stations show subsidence at rates of about 1.7 cm/year in the first 1.5 and 2 years after the earthquake (e.g., Yamagiwa et al. 2015; Hu et al.
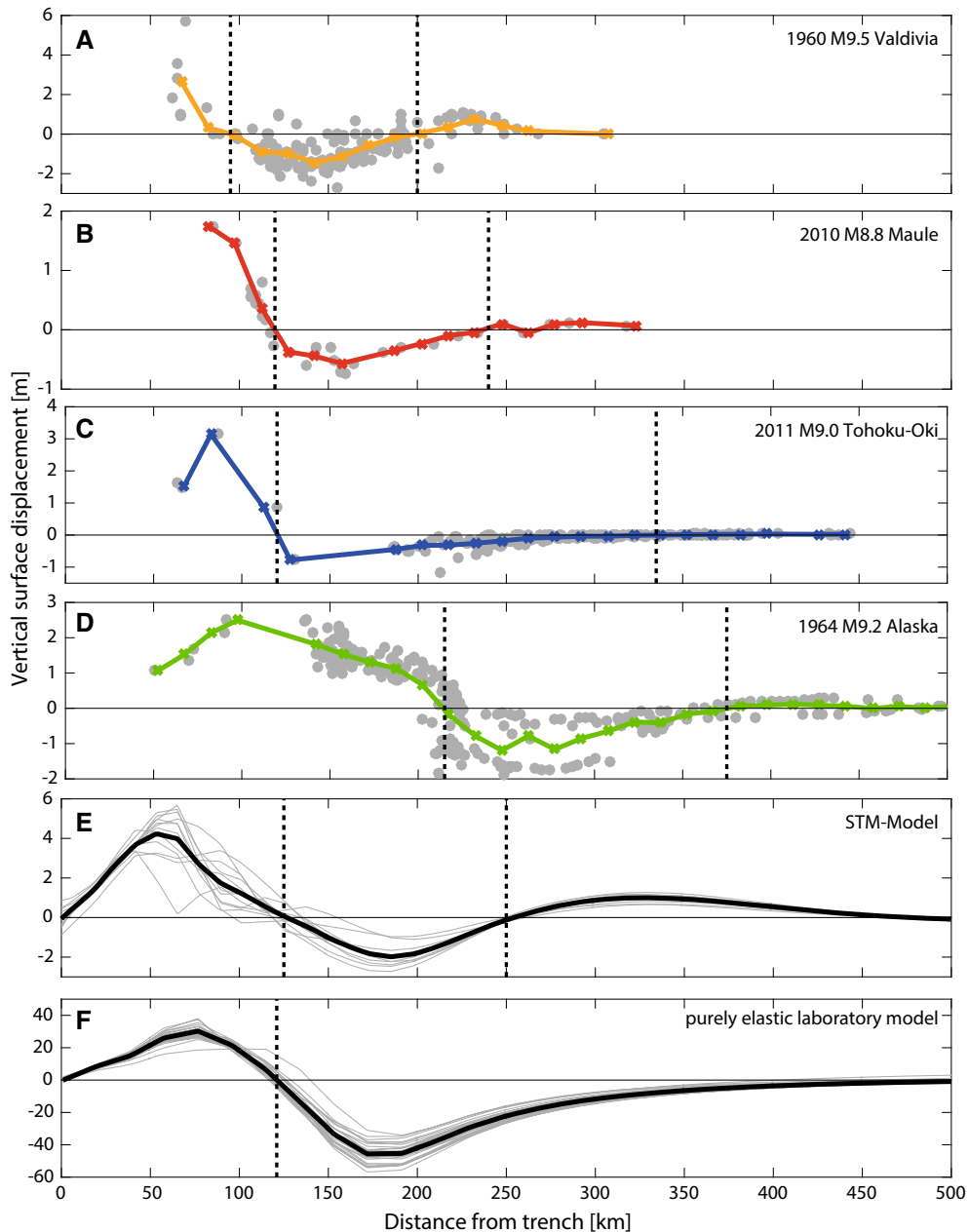
Figure 3

Cross section showing the coseismic subsidence and uplift for the **a** 1960 M9.5 Valdivia, **b** 2010 M8.8 Maule, **c** 2011 M9.0 Tohoku-Oki, **d** 1964 M9.2 Alaska earthquakes, **e** our seismo-thermo-mechanical (STM) models, and **f** a purely elastic laboratory-scale model. Various amounts of postseismic displacements can be included in these coseismic estimates (see Table 1; Sect. 4.1). Gray dots are data points located at each measurements minimum distance to the trench to account for along-strike variations of long trenches. Bold colored lines represent their means as binned over widths of 15 km. For the model gray lines represent individual events and black lines are means. The solid black line is zero vertical displacement and the dotted vertical lines indicate the two hinge points HP_1 and HP_2, where the surface displacement changes from uplift to subsidence and vice-versa. Note the different vertical scales. All earthquakes and the STM model show a secondary zone of uplift, but its amplitude and the position of HP_2 varies. The surface displacements of the purely elastic model asymptotically go to zero for large distances to the trench
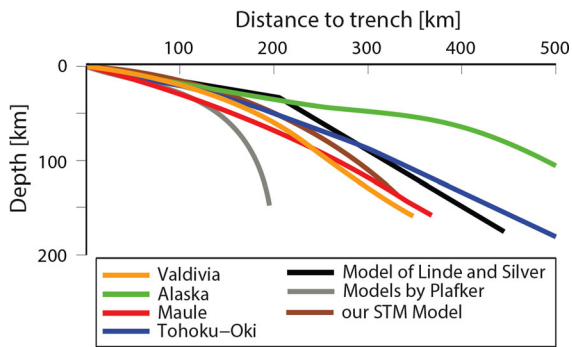
Figure 4
Cross section of slab depths from Slab1.0 (Hayes et al. 2012) and from models discussed in the text, showing how different the slabs are dipping in both nature and models

2016). This opposite direction of vertical displacements in Japan and Chile and the significantly decreasing uplift rates for Chile suggest that the zone of postseismic uplift in the midfield and the secondary zone of mostly coseismic uplift could be different features, which may overlap.

3.2. Seismo-thermo-mechanical models predict a secondary zone of uplift

To understand the universality and physical origin of the secondary zone of uplift we first analyze its evolution and characteristics in the realistic Southern Chile model setup (Fig. 1a). The model simulates 36 spontaneous, largely quasi-characteristic and quasi-periodic events during which on average the overriding plate displaces by about 18 m every 881 years. The surface displacements of the reference model reproduced the spatial pattern of vertical displacements for the 2010 M8.8 Maule earthquake unintentionally and without any tuning due to its physically-consistent basis (Fig. 5 in van Dinther et al. 2013b, which also corresponds to a grey line in Fig. 3e). They show a distinct secondary zone of uplift beyond $\sim$ 250 km from the trench with a peak around 330 km. Here, we analyze additional events of this same model (grey lines in Fig. 3e). Events are detected based on the slip velocity, i.e. the coseismic phase starts when the markers located just above the interface start to move significantly seaward and end when they return to pre-event levels. The resulting displacements and hinge points in Fig. 3e agree well

with the reference event of van Dinther et al. (2013b, Fig. 5 therein) and all show a secondary zone of uplift. The consistency of the location of the secondary zone of uplift for different events is notable and seems fairly independent of event details and rupture size. The limited amount of smaller events in the sequence causes minor variations in the pattern of uplift in the primary zone, while variations in the secondary zone of uplift are rather negligible.

The universal nature of the secondary zone of uplift is supported by extensive tests in which this realistic setup was more and less drastically changed in attempts to remove the secondary zone of uplift. In these tests we have taken care to ensure that the secondary zone of uplift is not influenced by numerical modeling parameters (e.g., domain size and boundary conditions). None of the tested numerical parameters influences the location and magnitude of the secondary zone of uplift in a noteworthy manner (e.g., compare red and blue lines with black lines in Fig. 5). Additionally, all models with a wide range of tectonic and material parameters reveal a secondary zone of uplift. These models will be discussed in more detail in Sects. 3.3.2 and 4.2 to better understand the physical mechanisms governing it.

To better understand what happens we analyze the spatiotemporal evolution of one quasi-characteristic event and one seismic cycle in detail (Fig. 6). Figure 6a portrays the vertical surface velocities as a function of distance to the trench (X) and time in time steps (Y). During the interseismic period the fore-arc within 100 km from the trench is dragged landward, since it is coupled to the landward subducting plate (also see spatial snapshots in Fig. 6b, d). This compression causes primary interseismic uplift of the overriding plate from about 100 to almost 300 km. Interestingly, a secondary zone of interseismic subsidence occurs at distances beyond 300 km from the trench. This model thus predicts very slow interseismic subsidence (i.e., less than mm/year) at a few hundred kilometers landward of the trench.

During the coseismic period accumulated displacements within the overriding plate are largely elastically rebound [see Fig. 5 in same models of van Dinther et al. (2013b), where on average more than 90% of interseismic displacements is rebound].
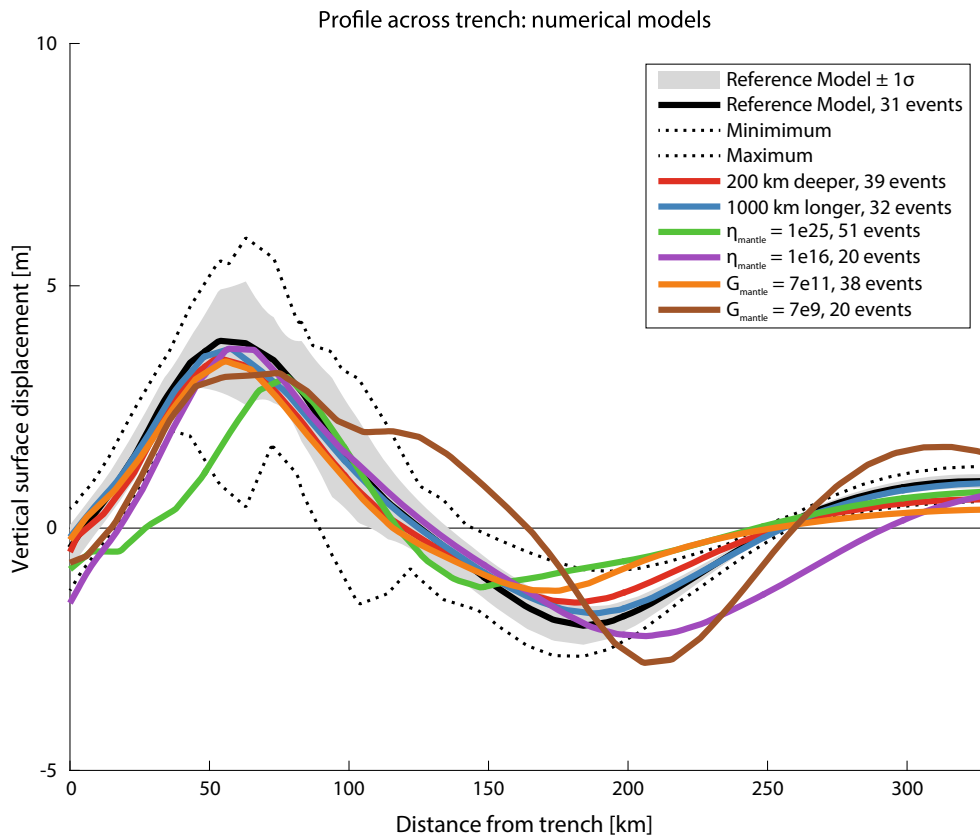
Figure 5
Vertical surface displacements accumulated over the coseismic period versus distance to the trench for different seismo-thermo-mechanical models. Black line (mean) and grey shading ($\pm 1\sigma$) represent the reference model with dashed lines showing the maximum and minimum of all events in the reference model. Colored solid lines represent the mean of different simulations, as calculated for the given number of events per simulation. Red and blue lines indicate simulations with a 200 km deeper (+ 100%) and a 1000 km longer model (+ 67%) respectively. Green and purple curves result from simulations with about five orders of magnitude larger and smaller viscosity in the mantle (the former only beneath the overriding plate). Orange and brown curves result from overriding mantle shear moduli respectively increased and decreased by one order of magnitude

Elastic rebound leads to a primary zone of uplift, which propagates seaward along with the rupture that nucleated just above the brittle-ductile transition. Behind this propagating uplift, the extending overriding plate experiences primary subsidence. Beyond about 250 km the secondary zone of uplift occurs (also see spatial snapshots in Fig. 6c, e). This uplift occurs over the same time period during which primary coseismic uplift occurs, although it lasts slightly longer. This suggests that the secondary zone of coseismic uplift at least has a distinct coseismic component, although exact distinctions are not allowed due to the low temporal resolution of the numerical model.

Analyzing velocities at depth shows that the secondary zone of uplift is connected to a broad pattern of uplift occurring throughout the whole lithosphere and mantle. Upward velocities occur landward of a dipping line connecting the secondary hinge point at the surface and the start of ductile deformation at the megathrust interface (T > 450 °C in Fig. 6e). The second hinge point at the surface is located roughly above the interplate decoupling point, which is located at the megathrust interface at depths of about 90–95 km. The interplate decoupling point marks the depth below which motions of the hanging wall decouple from those in the footwall, which from then on induce corner flow in the mantle
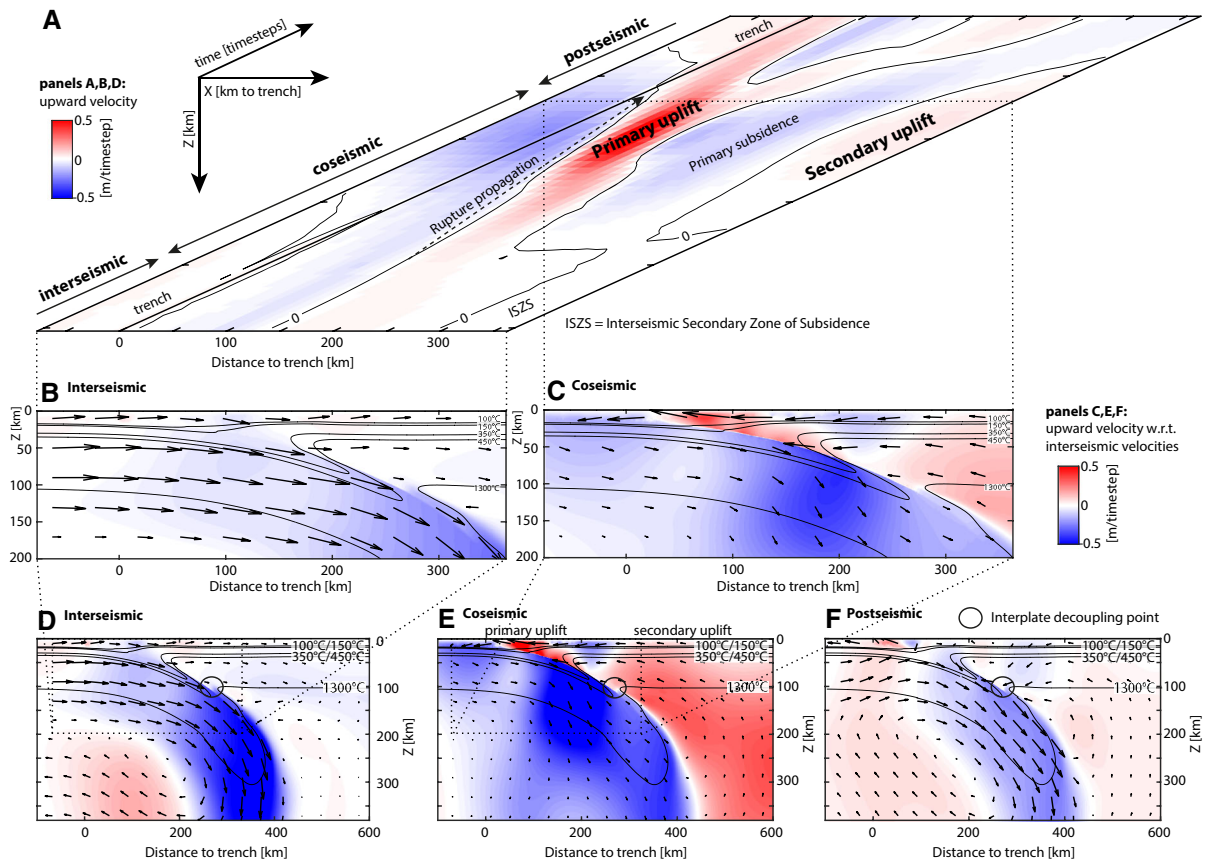
Figure 6

a Evolution of vertical surface velocities through space (Y) and time (X). Contours indicate separation of regions of uplift and subsidence. Note that the time axis is spaced in terms of time steps (five time steps per dash) with labels indicating duration of inter-, co- and postseismic periods. Values for time and coseismic velocities are not appropriate (resp. too long and slow) due to a constant time step of 5 years. The accumulated coseismic displacement due to the coseismic vertical velocities are shown in Fig. 5. Spatial cross-sections in the X–Z plane shown at inter- (**b**, **d**), co- (**c**, **e**) and postseismic (**f**) times. The middle panels (**b**, **c**) show zooms over the width shown in **a**, while lower panels (**d**–**f**) show larger cross sections revealing lithospheric and mantle flow patterns

wedge [definition updated from Furukawa (1993) starting with van Dinther et al. (2013b)]. This is evident from seaward flow in the astenosphere, as opposed to interseismic landward displacement of the lithosphere (Fig. 6d). This is facilitated by significantly decreased overriding plate viscosities due to ambient temperatures approaching 1300 °C. This roughly corresponds to the thermal definition of the lithosphere–astenosphere boundary within the overriding plate. At depth, corner flow is driven by slab penetration continuously, although at variable speeds (Fig. 6d–f). Subduction and slab penetration are slow within the interseismic period. As the megathrust interface decouples during an earthquake, subduction

and slab penetration are considerably accelerated. Displacements of the subducting plate are thus not rebound to their original position, but rather subduct faster to catch up with long-term subduction rates.

After the rupture arrests and the seismogenic zone relocks itself, postseismic velocities largely change back toward their interseismic pattern (also see spatial snapshot in Fig. 6f w.r.t. Fig.6d). This reversal is delayed within 50 km from the trench due to afterslip in the velocity-strengthening domain and beyond about 400 km from the trench due to viscous relaxation of the lithosphere–astenosphere. Additionally, the secondary zone of interseismic subsidence starts around 250 km, while it moves progressively
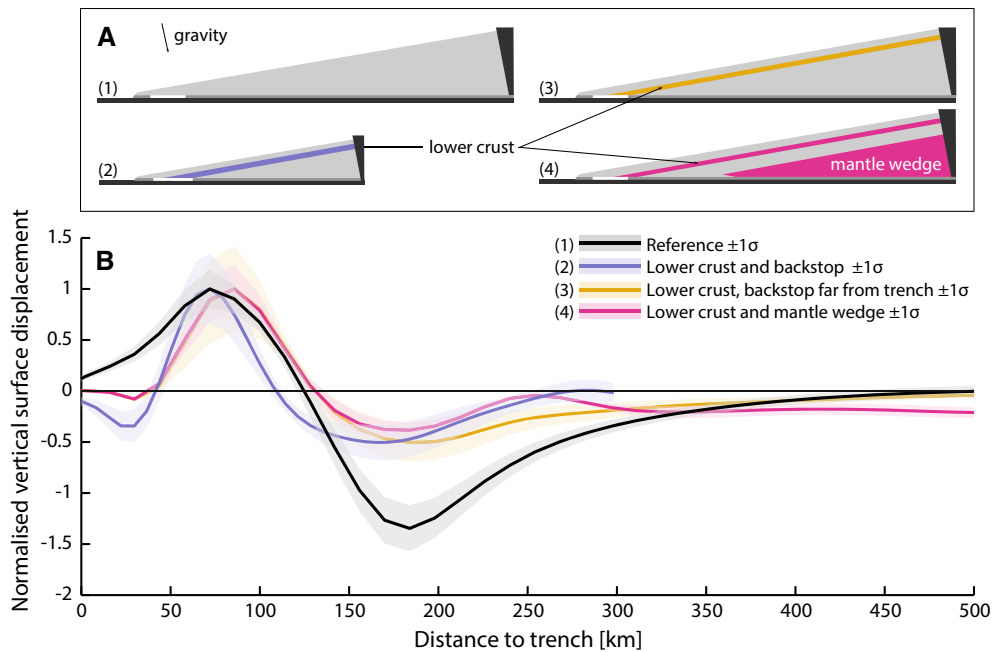
Figure 7

a Setups of laboratory-scale models that progressively increase in complexity: (1) dominantly elastic fore-arc, (2) add a visco-elastic lower crust with laboratory backstop, (3) move backstop to far-field, and (4) add a visco-elastic mantle wedge. The rheological layers are adopted from the large-scale thermo-mechanical model (Fig. 1a). **b** The resulting displacements of these models with uncertainties. To highlight the different shapes and not the amplitudes, the vertical displacements are normalized with respect to maximum primary uplift

downdip until it starts around 300 km in the late interseismic period.

3.3. Physical Mechanisms Governing a Secondary Zone of Uplift

Both observations from nature and results from our numerical models suggest that a secondary zone of uplift is a universal characteristic of great megathrust earthquakes. Here we attempt to identify possible physical mechanisms that are applicable to all subduction zones. To identify and directly test the proposed physical mechanisms we utilize two model setups (Sect. 2.3, Fig. 1). We aim to add a secondary zone of uplift to the simple elastic laboratory wedge setup, which simulates the classical model for surface displacements and thus does not include a secondary zone of uplift (Fig. 3f). Excluding an identified potential physical mechanism should also be able to remove the secondary zone of uplift from the realistic, albeit complex setup for Southern Chile (Fig. 3e). Satisfying both these criteria provides a

valid test for potential mechanisms, which discarded several potential mechanisms from acting at all or acting alone.

3.3.1 Elastic Rebound After Interseismic Buckling of Visco-elastically Layered Lithosphere

We start from the most simple setup, where a rigid slab subducts beneath a wedge-shaped fore-arc (van Dinther et al. 2013a) (Figs. 1b, 7a). When the fore-arc is homogeneous and virtually elastic, spontaneous cycles of megathrust events confirm results of elastic models with near trench uplift followed by subsidence (Fig. 7; a1 and black line in b). At large distances from the trench, the surface keeps subsiding, as it asymptotically approaches the zero level. Model sets 2, 3 and 4 shown in Fig. 7 demonstrate how this subsidence in the elastic model is modified by adding essential model complexities.

Model set 2 introduces a lower crustal layer with reduced viscosity in the original analogue model

setup, which introduces a very small secondary zone of uplift around 250–300 km from the trench (cf. sets 1 and 2 in Fig. 7b). This modulation is related to the presence of a thin elastic beam (i.e., the upper crust) separated by a viscously deforming layer (i.e., the lower crust). The thin elastic beam is then free to buckle during the interseismic period in response to horizontal compression due to an end load (e.g., Turcotte and Schubert 2002). Elastic buckling due to horizontal forces typically introduces a secondary zone of subsidence at large distances from the trench (e.g., Fig. 6a). This zone of secondary subsidence is approximately rebound in the coseismic period due to reversal of elastic deformation (e.g., Reid 1910), thereby introducing a secondary zone of uplift. Buckling is not observed in the original model with the thick overriding plate (model 1 in Fig. 7b), since the horizontal compressional forces are not large enough to buckle a thick beam with a very large elastic thickness.

Model set 3 shows a gentle secondary zone of uplift reduces to a secondary zone of slight relative uplift, albeit absolute subsidence, when the backstop is moved further inland (Fig. 7a3, b). This suggests that, for buckling to be effective in introducing secondary uplift, a means to generate more localized compression is needed. A backstop corresponds to a region that is significantly stronger than the region just trenchward of it. This can result from a transition from sedimentary to magmatic/metamorphic rocks (Byrne et al. 1993) or a transition from thinner, warmer and weaker arc lithosphere to colder, thicker and stronger (e.g., cratonic) lithosphere (Sobolev and Babeyko 2005; Manea et al. 2012). However, it is arguable whether a backstop is present at the required location in all subduction settings. It is also only modestly present at a location closer to the trench in the large-scale model, which also simulates a secondary zone of uplift.

When a viscous mantle wedge is added in set 4, a minor kink in the reduced subsidence curve of set 3 is turned into a clear, albeit still subsiding, secondary bulge (Fig. 7a4, b). This is added to reproduce the mechanical structure of the overriding plate in the large-scale model (Fig. 1a). A weak lower crust and weak mantle wedge create a double-beam system made of the rigid upper crust (upper beam) and

mantle lithosphere (lower beam). This facilitates additional buckling of the lithospheric mantle and thus leads to a higher-order wavelength of surface displacements. Note here that the peak of the secondary bulge is roughly located above the mantle wedge tip, which colocates with the interplate decoupling point. This peak, however, remains below the zero vertical displacement level and the surface at 200–300 km is thus still subsiding.

3.3.2 Need for a Second Mechanism

Numerical experiments in the analogue model setup show elastic rebound following interseismic horizontal compression of a visco-elastically layered lithosphere is able to introduce a high-order buckling wavelength. However, in several dozens of attempts widely varying mechanical structure through geometries and parameters, we are not able to generate a consistent secondary zone of uplift with amplitudes above the zero level. Our summarized results in Fig. 7b show that a mechanism to generate broad uplift over larger wavelengths is missing. A rigid backstop in the near field (i.e., within 300 km) might be able to facilitate this for some events, although adding that to an analogue setup with complete visco-elastic layering still only partially ensures elevations above zero. However, the disputable presence of a backstop at those locations in both nature and our large-scale models suggests that a second mechanism is needed.

The need for a second mechanism is confirmed in dozens of experiments in a large-scale setup. A secondary zone of uplift can not be removed by eliminating the thin rigid beam structure that facilitates buckling of the overriding plate. Increasing viscosities of the lower crust and/or upper mantle on the landward side to 10^{25} Pa s shows that surface displacement patterns are affected to a minor extent, so that a secondary zone of uplift remains present and largely unchanged (green line in Fig. 5). This also suggests that, at least in the the analogue setup, visco-elastic relaxation within the hanging wall is not a key mechanism. Besides this experiment we ran numerous experiments in the large-scale model aimed to remove the secondary zone of uplift. None of these experiments lead to removing of the secondary zone
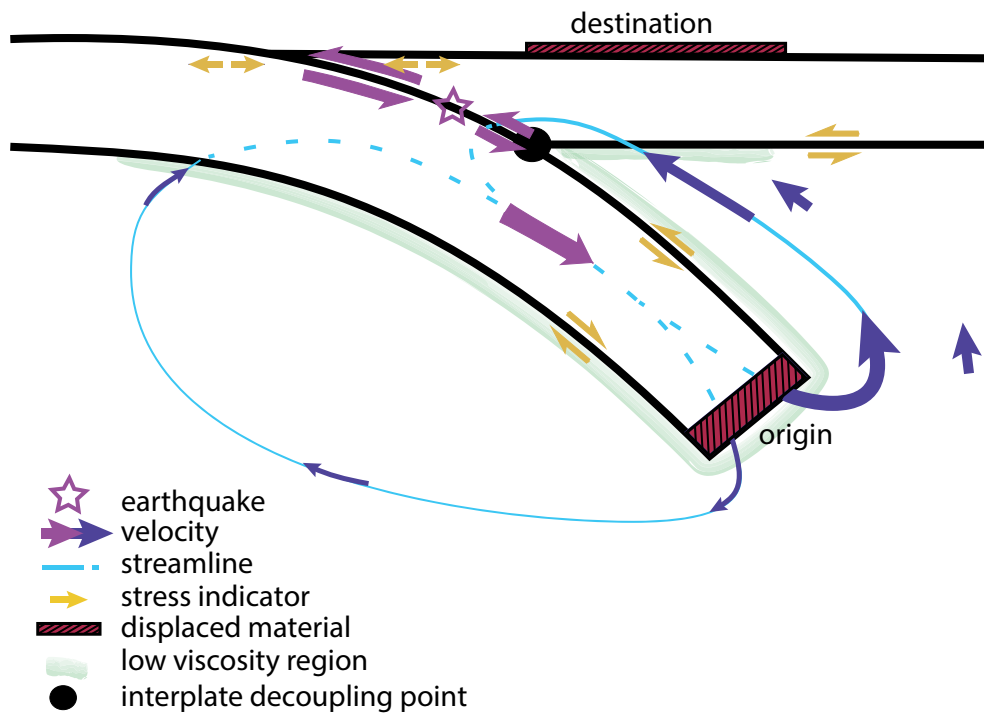
Figure 8
Schematic diagram illustrating how mass conservation due to accelerated slab penetration causes a secondary zone of uplift. Black lines represent lithosphere contours and other colors are described in the legend

of uplift, while generally its amplitude and location remained largely unchanged (a few selected experiments are shown in Fig. 5). This wide range of experiments rather shows that the second mechanism is a very basic feature of our model that can not be removed. One option that is difficult to quantify is the presence of a smoothly curved interface. However, since we do not observe a secondary zone of uplift in other smoothly curved models (e.g., Moreno et al. 2009) we suspect curvature is not the key component. If this holds, then the only other mechanism not present in our analogue model involves the slab and mantle kinematics and dynamics.

3.3.3 Mass Conservation Following Slab Penetration

To analyze the impact of subduction dynamics, we return to the spatial cross sections (Fig. 6d–f) and schematically represent our interpretation of the physical mechanism in Fig. 8. Interseismic velocities show relatively slow slab subsidence and motion

towards the land, which drags along and compresses the overriding plate (Fig. 6b, d). During an event the seismogenic zone unlocks and accumulated overriding plate displacements rebound, whereas the slab instead accelerates downward (Fig. 6c, e). This penetration represents the footwall displacements of the thrust event and ensures that the slab at depth catches up with its long-term subduction rates, since subduction was partially stalled during the interseismic period due to locking at the megathrust interface (see velocity variations in oceanic domain in Appendix Fig. 10a, b). These coseismic displacements of the slab are comparable in size to those in the less constrained overriding plate (compare arrows in supplementary movie S1), which is likely due to catching up of interseismic loading and slab pull. Coseismic slab displacements are thus considerable and on the order of a few tens of meters. For a 150 km wide downgoing region in two dimensions this amounts to a displacement of mantle material of a few square kilometers (red dashed area in Fig. 8 indicated as "origin"), which needs to be displaced

somewhere to conserve mass (and momentum). These large amounts of mantle are preferentially forced upward beneath the overriding plate (Figs. 6e, 8; Appendix Fig. 10b). This generates uplift on the landward side of the interplate decoupling point, which is mostly focused within 100–150 km landward of that (red dashed area in Fig. 8 indicated as "destination", i.e., the area of the secondary zone of uplift). These motions also uplift the lithosphere, where—at the same time—space is being created by the seaward displacements of the lithosphere. A simple calculation as suggested by Fig. 8 indicates that conserving the mass displaced as calculated above can lead to uplift on the order of tens of centimeters. In addition a smaller portion of mantle is displaced upward beneath the oceanic plate (Appendix Fig. 10b). These displacement patterns form two (tilted) convective cells similar to what is observed if mass is conserved due to a sinking object [see Fig. 1.2b in Gerya (2010)]. These two convective cells become more narrow and more clear in the postseismic phase (Fig. 6f). Finally, this mechanism can be better understood through an analogy in which you put your finger into a pot with honey and as a results of this the surface surrounding your finger is slightly uplifted.

In summary, both interseismic buckling of a double-beam overriding plate and upward mass-conservation driven flow in the mantle wedge are necessary to produce a secondary zone of uplift due to megathrust earthquakes.

3.4. Parameter Study

Lithosphere buckling and upward flow due to slab penetration suggest that the most influential parameters are related to the geometry of the fore-arc as well as slab and seismogenic zone geometry. This agrees with our preliminary findings based on the limited observations from nature, where the geometries of the slab interface and rupture seemed most important (Sect. 3.1).

To analyze the role of these geometries in a physically-consistent manner, we varied the slab age. This primarily affects the thermal structure within the slab and thus the megathrust geometry and seismogenic zone width. An older slab has more time to cool

and thus leads to lower temperatures at the megathrust interface and a deeper and slightly wider seismogenic zone (especially for the young slabs; see legend Fig. 9a). Ruptures in a wider seismogenic zone penetrate more landward and thus cause subsidence and extension further land inward, thereby leading to a landward shift of the spatial surface pattern and the second hinge point (Fig. 9a, b). Figure 9c shows that peak amplitude of the secondary zone of uplift hardly changes with slab age or downdip rupture limit. This is likely due to the fact that the seismogenic zone width only weakly increases with slab age (see legend Fig. 9a), such that maximum earthquake size increases only weakly.

We further analyze the role of event magnitude by also including other presented models to allow for a larger variation in earthquake size . We find that the location of the second hinge point is not correlated to event magnitude (Fig. 9d). The amplitude of the secondary zone of uplift does appear to increase with increasing earthquake size and slip (Fig. 9e).

Summarizing observations from nature and our models, the geometry of the secondary zone of uplift is mostly influenced by the geometry of the seismogenic zone (i.e., its dip and resulting downdip rupture limit).

4. Discussion

We first confirm the existence of a secondary zone of uplift both from an observational and numerical modeling perspective. We then hypothesize on the physical mechanisms governing this secondary zone of uplift and propose that two complementary mechanisms are needed. First, elastic rebound from interseismic buckling of a visco-elastic layered lithosphere due to horizontal compression to generate a wave length. Second, conservation of mass due to accelerated slab penetration to generate (focused) uplift. This section discusses the limitations, embedding of mechanisms within the literature, open challenges and implications of this.
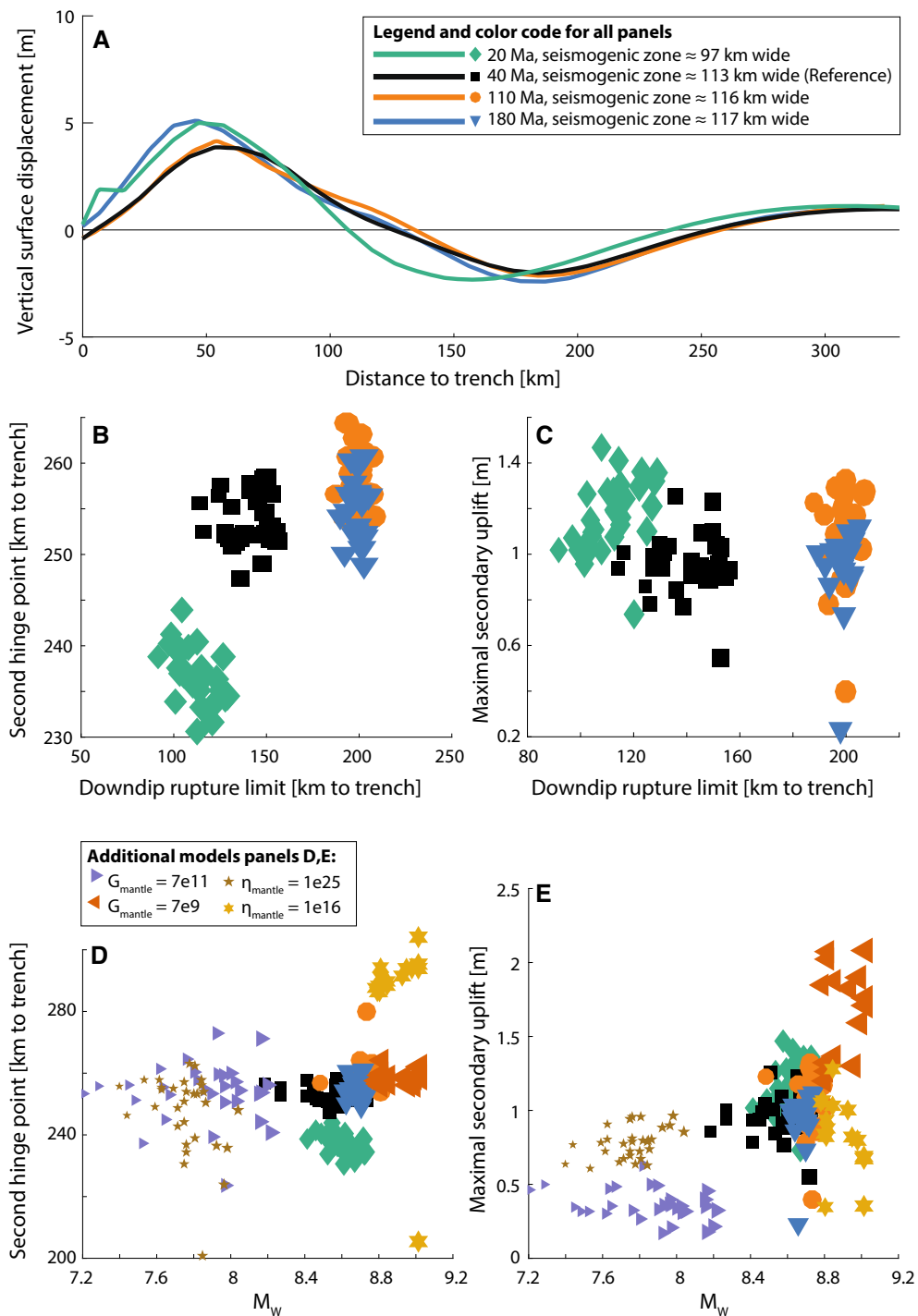
Figure 9
a Displacements of models with different slab ages showing a landward shift of the second hinge point for older slabs. **b** The downdip rupture limit and the second hinge point are clearly correlated. **c** The amplitude of the uplift is not related to downdip rupture limit and therefore slab age. **d** Models with distinctly different mantle parameters show that the second hinge point does not depend on the magnitude of the event. **e** The maximal secondary uplift however is related to the magnitude of the events

4.1. Limitations

The 2D STM models are able to model both long-term subduction dynamics and short-term seismogenesis. This innovation allows them to predict new features and processes, which previously went either not observed or unrecognized. One such example is this consistent presence of a secondary zone of uplift due to megathrust earthquakes. The challenge of bridging all relevant time scales of subduction zone processes has, however, not been fully completed and thus involves some limitations for the large-scale model (section 4.6, van Dinther et al. (2013b)). The main limitation is the exceptionally long coseismic duration of our events (years instead of seconds), which does not allow us to seperate postseismic and steady-state subduction contributions from the coseismic contribution. The same problem holds for natural data from the two earthquakes in the 1960s, since measurements were done years after the earthquakes. A second, relevant modeling limitation lies within the applied rheologies. These models use the assumption of incompressibility, which is a typical assumption made in geodynamic models. Compressibility could decrease the surface response due to accelerated slab penetration, although elimination of this characteristic response is not expected (as supported by similar motions in Sun and Wang (2015) for a Poisson's ratio of 0.25). These limitations have been overcome using adaptive time stepping, rate-and-state friction and compressibility in large-scale models of strike-slip settings (Herrendoerfer et al. 2018). However, bridging from millions of years of subduction to earthquake dynamics remains a challenge (Herrendoerfer 2018). This is thus far only partially accomplished by coupling two different models (van Zelst et al. 2019) or for resolving the postseismic phase (Sobolev and Muldashev 2017).

4.2. Embedding of Proposed Mechanisms

The proposed physical mechanisms form a new universal explanation for a secondary zone of uplift and for related modeled displacement patterns. In this section we compare our mechanisms and displacement patterns to other studies and start discussing open questions. Other studies with a (visco-)elastic

rheology do typically not discuss a secondary zone of uplift (e.g., Wang 2007). Interestingly, also large-scale models of Miyashita (1987) reveal a secondary zone of coseismic uplift, which is also followed by subsidence that propagates landward in the postseismic phase.

In terms of physical mechanisms, the fact that they are universal and apply to all subduction zones is important, because we demonstrated its universal existence for various types of subduction zones. That suggests that a mechanism should not be valid only for one or two subduction zones, but rather for all. Hence the specific geometrical causes to locally uplift material due to abrupt curved steepening of this interface (Plafker and Savage 1970) or distinct slab interface kinks (Linde and Silver 1989) are not deemed relevant for all subduction zones. Moreover, a compilation of slab data rather shows smooth interfaces without such rapidly changing slab shapes (Fig. 4 based on data from Hayes et al. 2012).

The first mechanism of interseismic buckling due to horizontal compression falls in the same category as the transverse crustal buckling of a horizontally compressed continental plate mentioned by Plafker (1972). We, however, emphasize that compression occurred during the interseismic period (not coseismic) and resulted in a secondary zone of subsidence. This was subsequently rebound during the earthquake and hence showed secondary uplift. Second, we added that a realistic visco-elastic layering of the lithosphere is needed to have a thin enough elastic beam that can buckle (Turcotte and Schubert 2002). The need of a realistically layered visco-elastic lithosphere to show higher-order wavelengths in vertical displacements has also been shown by Pollitz (1997). Besides inducing lithospheric buckling through horizontal forces, Vita-Finzi and Mann (1994) modeled buckling and a primary and secondary zone of uplift of an elastic beam atop a viscous asthenosphere due to vertical forces (i.e., flexure). These oscillations resulted largely from buoyancy effects following mass displacements within which accelerated subduction lead to overlap and a positive buoyancy force that uplifts the primary zone. In our model density displacements are different and it is rather elastic rebound from an overriding plate that is dragged down with the slab that causes

primary uplift. Instead secondary uplift seems to result from a superposition of horizontal buckling and slab-induced return flow.

The second mechanism of accelerated slab penetration and resulting accelerated convection to conserve mass is new. However, the resulting convective displacement patterns throughout the lithosphere-mantle system are similar to those modeled in Sun et al. (2014); Sun and Wang (2015) [see Fig. 3A in Sun and Wang (2015)]. They, however, explain all displacements using the general term of visco-elastic relaxation and appoint an asymmetric rupture inducing greater tension in the upper plate as driving mechanism for these convective displacements with two cells. In our model the rupture is much more symmetric (Fig. 6e) as the slab moves more and thus induces stress changes that are comparable [see Fig. 3D in van Dinther et al. (2013b)]. Larger slab displacements are likely caused by more realistic cyclic loading of our self-consistent system [and presence of spontaneous low viscosity zones around the slab as in Figs. 1a, 8 and maybe off-fault plasticity (van Dinther et al. 2013b)]. Realistic interseismic loading ensures the relatively compressed slab catches up with slab pull in the coseismic period as subduction was partially inhibited in the interseismic period. Additionally, long-term subduction causes a pre-stress state with large extensional stresses in the slab and near neutral (locally compressional) stresses in the wedge. Nonetheless, we still interpret that rapid seaward motion of the wedge contributed, since these convective displacements fill up the space created by the seaward displaced wedge. Instead, as a primary control, slab penetration creates accelerated uplift as mass (and momentum) are conserved. Secondary, this uplift is tunneled towards the displaced wedge and creates a secondary zone of uplift (Fig. 8). This slab penetration mechanism might also be relevant for visco-elastic relaxation and should be considered and explored in physical explanations of it.

Our choice to not refer to this mechanism as visco-elastic relaxation per se is supported by experiments showing that a secondary zone of uplift also occurs when the overriding mantle deforms elastically (green line in Fig. 5). Therefore the ability of the visco-elastic mantle to delay and relax overriding plate displacements does not seem critical for a secondary zone of uplift. Instead letting the astenospheric mantle largely deform viscously does not remove its presence either, although it distinctly shifts the secondary zone of uplift in the direction of the land (purple line in Fig. 5). This could reflect a more distinct contribution from elastic rebound following interseismic buckling.

This second mechanism could be crudely related to a transient and coseismic version of the long-term thin viscous sheet model combined with corner flow that uplifts the volcanic arc (Wdowinski et al. 1989), as remarked upon by Vita-Finzi and Mann (1994). It namely relates to the corner flow of the mantle as induced by subduction to uplift a deformable lithosphere. We observe corner flow during the interseismic period (Appendix Fig. 10a). However, the displacement pattern of its accelerated version during coseismic slab penetration is distinctly skewed towards the seaside as the overriding plate is displaced in that direction (Appendix Fig. 10b). In addition our uplift is rapid and thus involves a larger elastic component.

It is possible that internal slab deformation and slab unbending due to the earthquake (around X = 300 km in Fig. 6c) could provide a minor contribution to this phenomenon. However, analysis of this phenomena demonstrated that it does not play an important role in our simulations. Additionally, these models can not exclude the role of deep afterslip in early postseismic displacements. It is implicitly included in the large-scale models in the form of dislocation creep (not frictional strengthening) in a spontaneous low viscosity channel from about 450° to 1300° (Fig. 1a). However, deep afterslip down to the interplate decoupling point rather seems to induce postseismic subsidence in the area of interest, just landward of the decoupling point (i.e., at 250–400 km in Fig. 6f). This sense of timing would support the dominance of two proposed mechanisms for a secondary zone of uplift during or shortly after megathrust earthquakes.

4.3. Coseismic or Postseismic Nature

The limited temporal resolution in the data and in the model make it challenging to decipher how much of the uplift in the secondary zone is coseismic and how much is postseismic in nature. However, the better resolved data during and following the 2010 M8.8 Maule and 2011 M9.0 Tohoku earthquakes suggest the secondary zone of uplift is mostly coseismic in nature. In the Maule region the coseismic data of Vigny et al. (2011) and postseismic data of Klein et al. (2016) combined show a strong decrease in uplift rates (Sect. 3.1.3). This decrease through time suggests that the small majority of the uplift occurred within the coseismic measurements of Vigny et al. (2011). The coseismic nature of the secondary zone of uplift is more evident for the Tohoku earthquake, where coseismic uplift on the west coast is followed by subsidence in the 2 weeks following the earthquake (Ozawa et al. 2011; Yamagiwa et al. 2015; Hu et al. 2016). Nonetheless, a relevant portion of the large amount of secondary uplift during the 1960 M9.5 Validivia earthquake was likely postseismic, since its tectonic setting is similar to the 2010 M8.8 Maule earthquake. In summary, we interpret that the secondary zone of uplift is coseismic in nature, whereas potential postseismic additions depend on the specifics of a subduction zone.

The numerical results can not unequivocally distinguish between coseismic and postseismic displacements, since the coseismic results likely contain a postseismic response due to the large time steps. However, the relative timing of surface displacements supports a mainly coseismic nature of the secondary zone uplift and the governing mechanisms. The relative timing is apparent from the simultaneous occurrence of a primary and secondary zone uplift (Fig. 6a). As the interface relocks and causes primary subsidence at around 50 km from the trench again, secondary subsidence starts to occur around 250–350 km from the trench as well.

It is open for discussion whether the second mechanism of mass conservation driven return flow (Fig. 8) occurs at coseismic and/or (early) postseismic time scales. Traditionally one might think that the response from the mantle will be too slow. However, we know that the mantle behaves elastically during and just after the earthquake, because of the prolonged propagation of seismic waves. Moreover, we know that mass must always be conserved, also when the large and heavy slab inevitably penetrates rapidly into the mantle. Together with the apparent occurrence of a mainly coseismic secondary zone of uplift, it seems this could occur at least during—or within the few days following—the earthquake. This might be observed on the Korean peninsula, where uplift is only observed for the five days following the 2011 M9.0 Tohoku earthquake (Kim and Bae 2012). Nonetheless, the penetration of the slab into the mantle will be at least partially delayed, since on both sides of the slab the mantle resists its penetration as it does for the overriding plate. The resulting shear stresses (Fig. 8) will need to be relaxed on the time scales mostly dictated by mantle viscosity. In our model these viscosities are low and on the order of 10^{18} Pa s (Figs. 1a, 8). This reduction with respect to the surrounding mantle with viscosities of about 10^{20} Pa s occurs due to increased strain rates around the slab, which feedback non-linearly via the stress dependence of dislocation creep viscosity (Eq. 2). Consequently, Maxwell relaxation times would be around one or a few years, unless accelerated slab penetration on time scales of minutes can increase them even further in the vicinity of the slab (e.g., to around 10^{15-16} Pa s as in Sobolev and Muldashev 2017). In summary, we estimate mass conservation following accelerated slab penetration operates on both coseismic and (early) postseismic time scales, where it may also affect visco-elastic relaxation. What contribution is coseismic and what is postseismic could also be affected by the specifics of a subduction zone.

4.4. Implications

These results imply that subduction is not a gradual process with subduction occurring at constant rates, as typically envisioned within the long-term communities. Subduction rather proceeds in shocks following the brittle stick-slip behaviour of the shallow seismogenic zone. During the interseismic period some subduction can occur. However, locking across a 100 km or 200 km portion of the megathrust interface can partially stall the penetration of the slab. When the whole megathrust unlocks during a great megathrust earthquake, subduction catches up and the

earthquake-induced displacement of the slab induces a significant amount of mantle flow (Fig. 6e, Supplementary movie S1). This makes megathrust earthquakes an integral driver of mantle flow. Similar ideas exploring the interaction between earthquakes and mantle flow are explored in other numerical models, which feature modulation of astenospheric flow (Barbot 2018) and modulation of residual polar wander (Cambiotti et al. 2016). This thus suggests a link between deep mantle and shallow surface displacements on timescales from minutes to decades, which is shorter than previously considered.

These numerical results also demonstrate implications for geodetic-based source inversions. The inclusion of visco-elastic layering and their detailed geometrical implementation distinctly impacts the resulting coseismic surface displacements (e.g., Fig. 7). Conversely, when using these surface displacements to estimate slip at a fault within a homogeneous elastic medium typically used for source inversions, one would artificially adapt fault slip to compensate for the missed partially viscous features. This is similarly observed for fitting interseismic velocity data, where elastic models require the presence of a rigid micro plate (e.g., Simons et al. 2007) that is not required using viscoelastic models (Trubienko et al. 2013). Additionally, slip artifacts might be introduced by the secondary zone of uplift present in data, but not in an elastic forward model. This might make it difficult to fit model results to the data (e.g., Lin et al. 2013, for the Maule earthquake). This supports emerging results that it is important to include a realistic visco-elastic structure in inversion for interseismic crustal deformation and earthquake slip inversions (e.g., Wang et al. 2012; Trubienko et al. 2013; Sun and Wang 2015; Klein et al. 2016; Moore et al. 2017; Sun et al. 2018).

4.5. Predicting Future Observations

Based on our observational and numerical findings, we make several predictions that can be tested as more accurate data becomes available during and prior to future, large megathrust earthquakes.

We predict more secondary zones of uplift will be observed in future great megathrust earthquakes (and maybe also for $M > 8$ or smaller earthquakes). The location of the secondary hinge point, its wavelength, its amplitude, and decay with time will vary with specifics of the various subduction zones (Figs. 3, 9). The location could move further inland for subduction zones with more shallowly dipping slabs, whose seismogenic zones are wider and earthquakes can thus penetrate more inland. More slip on the deep portion of the seismogenic megathrust likely also translates into higher amplitudes of secondary uplift. The contribution from interseismic buckling would be enhanced by the presence of more effective backstops (Fig. 7) and by compression of a thinner upper crust and/or mantle lithosphere [as eq. 3-124 in Turcotte and Schubert (2002) predicts lower amplitudes at larger distances]. The contribution of mass-conserving return flow due to slab penetration would be enhanced by increased uplift amplitudes when more slab material displaces more mantle and effectively tunnels it to just landward of the interplate decoupling point (Figs. 6e, 8). This is anticipated for subduction zones with slabs (and events) that have a larger lateral extent and/or larger thickness of the slab (as to some extent occurs for an older and cooler slab). Additionally, more slip also displaces more material that needs to be relocated.

Finally, we predict a secondary zone of interseismic subsidence to occur at similar distances of between 200 and 500 km from the trench (Fig. 6a). This interseismic subsidence will be very slow (Fig. 6d) and is the counterpart or cause that—through elastic rebound—leads to a secondary zone uplift due to megathrust earthquakes. It likely occurs just on the landward side of the interplate decoupling point, where mantle displacements beneath the overriding plate become dominant. This lithosphere - astenosphere transition facilitates both interseismic buckling and rapid upward displacements following slab penetration.

5. Conclusions

We propose to extend the classical earthquake vertical displacement pattern for great megathrust earthquakes from one to two zones of uplift that flank a zone of primary subsidence. A second, minor zone of uplift was first predicted by physically consistent models starting to bridge long- and short-term dynamics. Subsequently we observed it for all four

great megathrust earthquakes studied. This secondary zone of uplift starts at distances between 200 km and 350 km (or 500 km) from the trench and varies in magnitude from a maximum of 0.4 to 11 decimeter.

Extensive numerical experiments in both realistic and simple setups could not identify a single physical mechanism that is able to respectively remove and add a secondary zone of uplift to the two setups. Instead we hypothesize that a superposition of at least two mechanisms is needed to generate a secondary zone of uplift. We need a visco-elastically layered fore-arc to form two thin rigid beams that can buckle elastically in response to horizontal compression due to end loading in the interseismic period. This introduces a higher-order wavelength with a secondary zone of very minor interseismic subsidence. Elastic rebound due to an earthquake then causes a secondary zone of relative uplift. This is uplifted above zero by displacements that conserve mass (and momentum) following the earthquake-triggered penetration of the slab into the mantle. These upward displacements particularly localize in the about 150 km's landward of the interplate decoupling point, which typically corresponds to the area of the secondary zone of uplift.

Recent postseismic data and coincident, albeit unresolved, timing in our numerical model point to a mainly coseismic nature of the secondary zone of uplift. Uplift in the region of interest can either be enlarged or decreased during the postseismic period depending on the specifics of a subduction zone. The exact coseismic and postseismic contributions in various subduction zones and corresponding processes remain to be confirmed.

We estimate that the most important parameters affecting the secondary zone of uplift are the seismogenic zone dip and (deep) coseismic slip magnitude and limit (or earthquake size). Predictions from our models in terms of in the future verifiable observations include more secondary zones of coseismic uplift (potentially also for smaller earthquakes) and a secondary zone of very minor subsidence for interseismic displacements. Additionally, we propose a suite of tectonic influences that could start to explain variations in its size and location. In any case a more accurate representation of the visco-elastic structure of the fore-arc helps to understand and invert for inter-, co- and postseismic displacements. Finally, our results imply that subduction is not a gradual processes, but that is rather accelerated and decelerated through seismic cycles following the slab penetration during great megathrust earthquakes. This suggests a link between deep mantle and shallow surface displacements at time scales as short as minutes.

Appendix A: Conservation Equations

To obtain horizontal velocity v_x, vertical velocity v_z, and pressure P we solve the conservation of mass and momentum as

$$\frac{\partial v_x}{\partial x} + \frac{\partial v_z}{\partial z} = 0 \qquad (5)$$

$$\frac{\partial \sigma'_{xx}}{\partial x} + \frac{\partial \sigma'_{xz}}{\partial z} - \frac{\partial P}{\partial z} = \rho \frac{Dv_x}{Dt} \qquad (6)$$

$$\frac{\partial \sigma'_{zx}}{\partial x} + \frac{\partial \sigma'_{zz}}{\partial z} - \frac{\partial P}{\partial z} = \rho \frac{Dv_z}{Dt} - \rho g. \qquad (7)$$

Here σ'_{ij} represents the 2D deviatoric stress tensor. The conservation of momentum includes gravitational acceleration g and the inertial term, represented by density ρ times the Lagrangian time derivative of the respective velocity components $\frac{Dv}{Dt}$. The momentum equations include the inertial term to stabilise high coseismic slip rates at low time steps (van Dinther et al. 2013a). A time step of five years, however, reduces our formulation to a virtually quasi-static one.

In the large-scale model we also solve the heat equation

$$\rho C_p \left(\frac{DT}{Dt} \right) = -\frac{\partial q_x}{\partial x} - \frac{\partial q_z}{\partial z} + H_a + H_s + H_r, \quad (8)$$

where C_p is isobaric heat capacity, DT/Dt is the Lagrangian time derivative of temperature, and q_x and q_z are the horizontal and vertical heat flux, respectively. The equation includes contributions from conductive heat transport and volumetric internal heat generation H due to adiabatic (de-)compression H_a, shear heating during non-elastic deformation H_s and lithology-specific radioactive heat production H_r (e.g., Gerya and Yuen 2003, 2007).

Appendix B: Large-scale velocities throughout the seismic cycle

Figure 10 shows how mantle flow is affected by slab penetration at each different stage in the seismic
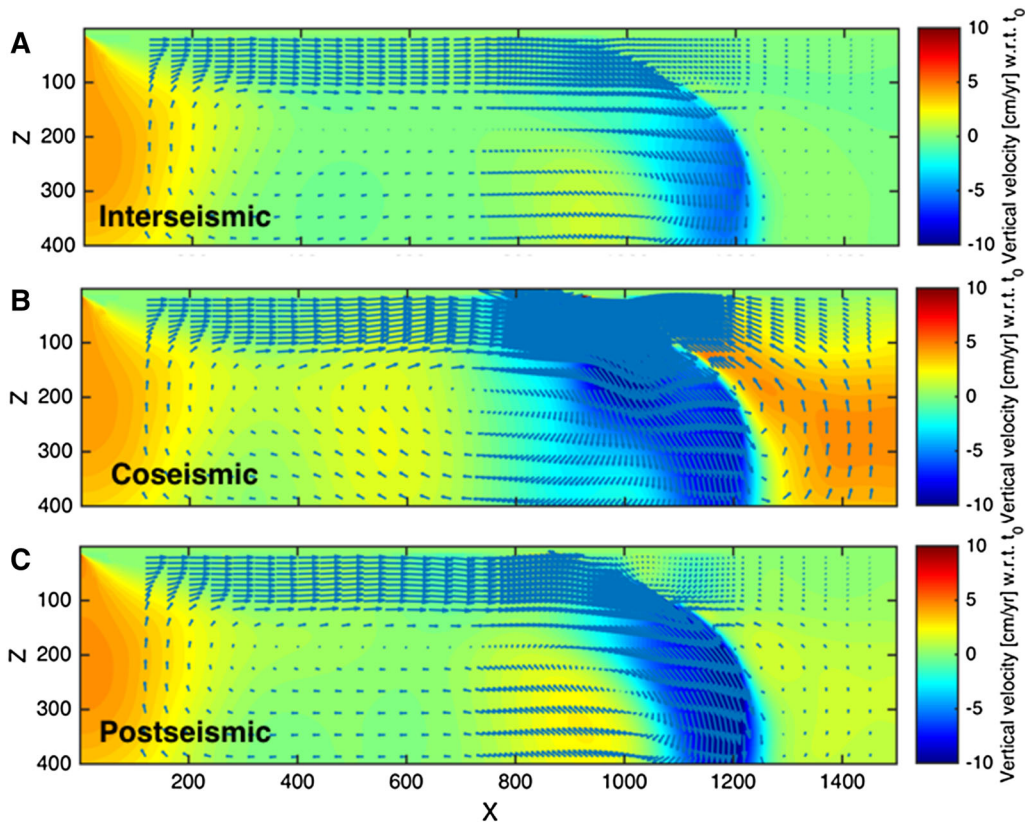

Figure 10
Snapshots of **a** interseismic, **b** coseismic, and **c** postseismic velocities throughout the whole model domain. This illustrates the reach and size of convective cells, which ensures mass is conserved as regular or accelerated subduction occurs. Colors indicate vertical velocities with respect to those at the start of the experiment

cycle. Accelerated slab penetration in the coseismic period leads to localized upward flow that is mainly returning on the landside of the slab. At the landside of the slab we also observe mantle flow is most focused within 150 km landward of the interplate decoupling point, where it could possibly fill up the space created by the displacement of the overriding plate.

Publisher's Note Springer Nature remains neutral with regard to jurisdictional claims in published maps and institutional affiliations.

REFERENCES

Barbot, S. (2018). Asthenosphere flow modulated by megathrust earthquake cycles. *Geophysical Research Letters*, *45*, 6018–6031.

Blaser, L., Kruger, F., Ohrnberger, M., & Scherbaum, F. (2010). Scaling relations of earthquake source parameter estimates with special focus on subduction environment. *Bulletin of the Seismological Society of America*, *100*(6), 2914–2926.

Byrne, D. E., Wang, W. H, & Davis, D. M. (1993). Mechanical role of backstops in the growth of forearcs. *Tectonics*, *12*(1), 123–144.

Cambiotti, G., Wang, X., Sabadini, R., & Yuen, D. (2016). Residual polar motion caused by coseismic and interseismic deformations from 1900 to present. *Geophysical Journal International*, *205*(2), 1165–1179.

Coffin, M. F., Gahagan, L. M, & Lawver, L. A. (1998). *Present-day plate boundary digital data compilation*. Tech. Rep. 174, University of Texas Institute for Geophysics. https://doi.org/10.1029/2005GL022437/full.

Corbi, F., Funiciello, F., Moroni, M.b., van Dinther, Y., Mai, P.M., Dalguer, L.A., Faccenna, C. (2013). The seismic cycle at subduction thrusts: 1. Insights from laboratory models. *Journal of Geophysical Research* *118*(4), 1483–1501. http://www.scopus.com/inward/record.url?eid=2-s2.0-84880710737&partnerID=40&md5=400ba823e2159242374c2b67a7d6639f.

Crameri, F., Schmeling, H., Golabek, G. J., Duretz, T., Orendt, R., Buiter, S., et al. (2011). A benchmark comparison of numerical topography—what are suitable sticky air parameters? *Geophysical Journal International*, *200*, 1–12.

Fujiwara, T., Kodaira, S., No, T., Kaiho, Y., Takahashi, N., & Kaneda, Y. (2011). The 2011 tohoku-oki earthquake: Displacement reaching the trench axis. *Science*, *334*(6060), 1240–1240.

Fukahata, Y. (2015). Afterslip and viscoelastic relaxation following the 2011 Tohoku-oki earthquake (Mw 9.0) inferred from inland GPS and seafloor GPS/Acoustic data. *Geophysical Research Letters*, *42*(1), 66–73. https://doi.org/10.1002/2014GL061735.

Furukawa, Y. (1993). Depth of the decoupling plate interface and thermal structure under arcs. *Journal of Geophysical Research Solid Earth (1978–2012)*, *98*(B11), 20005–20013. https://doi.org/10.1029/93JB02020.

Gerya, T. (2010). *Introduction to numerical geodynamic modelling*. Cambridge: Cambridge University Press.

Gerya, T. V., & Yuen, D. (2003). Characteristics-based marker-in-cell method with conservative finite-differences schemes for modeling geological flows with strongly variable transport properties. *Physics of the Earth and Planetary Interiors*, *140*(4), 293–318.

Gerya, T. V., & Yuen, D. A. (2007). Robust characteristics method for modelling multiphase visco-elasto-plastic thermo-mechanical problems. *Physics of the Earth and Planetary Interiors,163*(1–4), 83–105. https://doi.org/10.1016/j.pepi.2007.04.015.

Govers, R., Furlong, K. P., van de Wiel, L., Herman, M. W., & Broerse, T. (2018). The geodetic signature of the earthquake cycle at subduction zones: Model constraints on the deep processes. *Reviews of Geophysics*, *56*(1), 6–49.

Hashimoto, M., Choosakul, N., Hashizume, M., Takemoto, S., Takiguchi, H., & Fukuda, Y., et al. (2006). Crustal deformations associated with the great Sumatra-Andaman earthquake deduced from continuous GPS observation. *Earth Planets Space,58*(2), 127–139. https://doi.org/10.1186/BF03353369.

Hayes, G. P., Wald, D. J., & Johnson, R. L. (2012). Slab1.0: A three-dimensional model of global subduction zone geometries. *Journal of Geophysical Research*, *117*(B1), B01302. https://doi.org/10.1029/2011JB008524.

Herrendoerfer, R. (2018). *Modeling of the slip spectrum along mature and spontaneously forming faults in a visco-elasto-plastic continuum*. PhD thesis, ETH.

Herrendoerfer, R., Gerya, T., & van Dinther, Y. (2018). An invariant rate-and-state dependent friction formulation for viscoelastoplastic earthquake cycle simulations. *Journal of Geophysical Research Solid Earth*, *123*(6), 5018–5051.

Heuret, A., Lallemand, S., Funiciello, F., Piromallo, C., & Faccenna, C. (2011). Physical characteristics of subduction interface type seismogenic zones revisited. *Geochemistry Geophysics Geosystems*. https://doi.org/10.1029/2010GC003230.

Holdahl, S.R., & Sauber, J. (1994). Coseismic slip in the 1964 Prince–William–Sound Earthquake—a new geodetic inversion. *Pure and Applied Geophysics, 142*(1), 55–82.

Hu, Y., Bürgmann, R., Uchida, N., Banerjee, P., & Freymueller, J. T. (2016). Stress-driven relaxation of heterogeneous upper mantle and time-dependent afterslip following the 2011 Tohoku earthquake. *Journal of Geophysical Research*, *121*(1), 385–411. https://doi.org/10.1002/2015JB012508.

Johnson, J. M., Satake, K., Holdahl, S. R., & Sauber, J. (1996). The 1964 Prince William Sound earthquake: Joint inversion of tsunami and geodetic data. *Journal of Geophysical Research*, *101*(B1), 523–532. https://doi.org/10.1029/95JB02806.

Karney, C. F. F. (2013). Algorithms for geodesics. *Journal of Geodesy*, *87*(1), 43–55. https://doi.org/10.1007/s00190-012-0578-z.

Kido, M., Osada, Y., Fujimoto, H., Hino, R., & Ito, Y. (2011). Trench-normal variation in observed seafloor displacements associated with the 2011 Tohoku-Oki earthquake. *Geophysical Research Letters*. https://doi.org/10.1029/2011GL050057.

Kim, S. K., & Bae, T. S. (2012). Analysis of crustal deformation on the Korea Peninsula after the 2011 Tohoku Earthquake. *Journal of the Korean Society of Surveying Geodesy Photogrammetry and Cartography*, *30*(1), 87–96.

Klein, E., Fleitout, L., Vigny, C., & Garaud, J. D. (2016). Afterslip and viscoelastic relaxation model inferred from the large-scale post-seismic deformation following the 2010 Mw8.8 Maule

earthquake (Chile). *Geophysical Journal International*, *205*(3), 1455–1472.

Li, S., Moreno, M., Bedford, J., Rosenau, M., Heidbach, O., Melnick, D., et al. (2017). Postseismic uplift of the Andes following the 2010 Maule earthquake: Implications for mantle rheology. *Geophysical Research Letters*, *44*(4), 1768–1776. https://doi.org/10.1002/2016GL071995.

Lin YN, Sladen, A., Ortega-Culaciati, F., Simons, M., Avouac, J. P., Fielding, E. J., et al. (2013). Coseismic and postseismic slip associated with the 2010 Maule Earthquake, Chile: Characterizing the Arauco Peninsula barrier effect. *Journal of Geophysical Research*, *118*(6), 3142–3159. https://doi.org/10.1002/jgrb.50207.

Linde, A. T., & Silver, P. G. (1989). Elevation changes and the Great 1960 Chilean Earthquake: Support for aseismic slip. *Geophysical Research Letters*, *16*(11), 1305–1308. https://doi.org/10.1029/GL016i011p01305.

Manea, V., Perez-Gussinye, M., & Manea, M. (2012). Chilean flat slab subduction controlled by overriding plate thickness and trench rollback. *Geology*, *40*(1), 35–38.

Meltzner, A. J., Sieh, K., Abrams, M., Agnew, D. C., Hudnut, K. W., Avouac, J. P., et al. (2006). Uplift and subsidence associated with the great Aceh-Andaman earthquake of 2004. *Journal of Geophysical Research*, *111*(B2), B02407–n/a. https://doi.org/10.1029/2005JB003891.

Miyashita, K. (1987). A model of plate convergence in southwest Japan, inferred from leveling data associated with the 1946 Nankaido earthquake. *Journal of Physics of the Earth*, *35*, 449–467.

Moore, J. D. P., Yu, H., Tang, C. H., Wang, T., Barbot, S., Peng, D., et al. (2017). Imaging the distribution of transient viscosity after the 2016 Mw 7.1 Kumamoto earthquake. *Science*, *356*(6334), 163–167.

Moreno, M., Bolte, J., Klotz, J., & Melnick, D. (2009). Impact of megathrust geometry on inversion of coseismic slip from geodetic data: Application to the 1960 Chile earthquake. *Geophysical Research Letters*, *36*(16), L16310. https://doi.org/10.1029/2009GL039276.

Moreno, M., Haberland, C., Oncken, O., Rietbrock, A., Angiboust, S., & Heidbach, O. (2014). Locking of the Chile subduction zone controlled by fluid pressure before the 2010 earthquake. *Nature Geoscience*, *7*(4), 292–296. https://doi.org/10.1038/ngeo2102.

Moreno, M., Rosenau, M., & Oncken, O. (2010). Maule earthquake slip correlates with pre-seismic locking of Andean subduction zone. *Nature*, *467*, 198–202.

Moresi, L., Dufour, F., & Mühlhaus, H. (2003). A Lagrangian integration point finite element method for large deformation modeling of viscoelastic geomaterials. *Journal of Computational Physics*, *184*(2), 476–497.

Ozawa, S., Nishimura, T., Suito, H., Kobayashi, T., Tobita, M., & Imakiire, T. (2011). Coseismic and postseismic slip of the 2011 magnitude-9 Tohoku-Oki earthquake. *Nature*, *475*(7356), 373–376. https://doi.org/10.1038/nature10227.

Plafker, G. (1965). Tectonic deformation associated with the 1964 Alaska earthquake. *Science (New York, NY)*, *148*(3678), 1675–1687. https://doi.org/10.1126/science.148.3678.1675.

Plafker, G. (1969). *Tectonics of the March 27, 1964 Alaska earthquake*. US Geological Survey Professional Paper 543-I, United States Geological Survey.

Plafker, G. (1972). Alaskan earthquake of 1964 and Chilean earthquake of 1960: Implications for arc tectonics. *Journal of Geophysical Research*, *77*(5), 901–925. https://doi.org/10.1029/JB077i005p00901.

Plafker, G., & Savage, J. C. (1970). Mechanism of the Chilean Earthquakes of May 21 and 22, 1960. *Geological Society of America Bulletin*, *81*(4), 1001–1030. https://doi.org/10.1130/0016-7606(1970)81[1001:MOTCEO]2.0.CO;2.

Pollitz, F. (1997). Gravitational viscoelastic postseismic relaxation on a layered spherical Earth. *Journal of Geophysical Research*, *102*(B8), 17921–17941.

Reid, H. F. (1910). *The California earthquake of April 18, 1906. Report of the State earthquake investigation commission*. Tech. rep., Carnegie Institution of Washington, Washington, D.C.

Sato, M., Ishikawa, T., Ujihara, N., Yoshida, S., Fujita, M., & Mochizuki, M., et al. (2011). Displacement above the hypocenter of the 2011 Tohoku-Oki earthquake. *Science (New York, NY)*, *332*(6036), 1395–1395. https://doi.org/10.1126/science.1207401.

Simons, W. J. F., Socquet, A., Vigny, C., Ambrosius, B. A. C., Haji Abu, S., Promthong, C., et al. (2007). A decade of GPS in Southeast Asia: Resolving Sundaland motion and boundaries. *Journal of Geophysical Research*, *112*(B6), 686–20.

Sobolev, S. V., & Babeyko, A. (2005). What drives orogeny in the Andes? *Geology*, *33*(8), 617–620.

Sobolev, S. V., & Muldashev, I. A. (2017). Modeling seismic cycles of great megathrust earthquakes across the scales with focus at postseismic phase. *Geochemistry Geophysics Geosystems*, *18*(12), 4387–4408.

Socquet, A., Peyrat, S., Ruegg, J. C., Métois, M., Madariaga, R., Morvan, S., et al. (2011). The 2010 Mw 8.8 Maule megathrust earthquake of Central Chile, monitored by GPS. *Science (New York, NY)*, *332*(6036):1417–1421. https://doi.org/10.1126/science.1204132.

Sun, T., & Wang, K. (2015). Viscoelastic relaxation following subduction earthquakes and its effects on afterslip determination. *Journal of Geophysical Research*, *120*, 1329–1344.

Sun, T., Wang, K., & He, J. (2018). Crustal deformation following great subduction earthquakes controlled by earthquake size and mantle rheology. *Journal Of Geophysical Research Solid Earth*, *123*(6), 5323–5345.

Sun, T., Wang, K., Iinuma, T., Hino, R., He, J., Fujimoto, H., et al. (2014). Prevalence of viscoelastic relaxation after the 2011 Tohoku-oki earthquake. *Nature*, *514*, 84–87.

Trubienko, O., Fleitout, L., Garaud, J. D., & Vigny, C. (2013). Interpretation of interseismic deformations and the seismic cycle associated with large subduction earthquakes. *Tectonophysics*, *589*, 126–141.

Turcotte, D. L., & Schubert, G. (2002). *Geodynamics*, 2nd edn. Cambridge University Press, Cambridge.

van Dinther, Y., Gerya, T. V., Dalguer, L. A., Corbi, F., Funiciello, F., & Mai, P. M. (2013a). The seismic cycle at subduction thrusts: 2. Dynamic implications of geodynamic simulations validated with laboratory models. *Journal of Geophysical Research*, *118*(4), 1502–1525. https://doi.org/10.1029/2012JB009479.

van Dinther, Y., Gerya, T. V., Dalguer, L. A., Mai, P. M., Morra, G., & Giardini, D. (2013b). The seismic cycle at subduction thrusts: Insights from seismo-thermo-mechanical models. *Journal of Geophysical Research*, *118*(12), 6183–6202. https://doi.org/10.1002/2013JB010380.

van Dinther, Y., Mai, P. M., Dalguer, L. A., & Gerya, T. V. (2014). Modeling the seismic cycle in subduction zones: The role and spatiotemporal occurrence of off-megathrust earthquakes.

Geophysical Research Letters, *41*(4), 1194–1201. https://doi.org/10.1002/2013GL058886.

van Zelst, I., Wollherr, S., Gabriel, A. A., Madden, E., & van Dinther, Y. (2019). *Modelling coupled subduction and earthquake dynamics*. https://doi.org/10.31223/osf.io/f6ng5,eartharxiv.org/f6ng5.

Vita-Finzi, C., & Mann, C. D. (1994). Seismic folding in coastal south central Chile. *Journal of Geophysical Research*, *99*(B6), 12289–12299. https://doi.org/10.1029/93JB03061.

Wang, K. (2007). Elastic and viscoelastic models of crustal deformation in subduction earthquake cycles. *The seismogenic zone of subduction thrust faults* (pp. 1–36). Columbia: Columbia University Press.

Wang, K., Hu, Y., & He, J. (2012). Deformation cycles of subduction earthquakes in a viscoelastic Earth. *Nature*, *484*, 327–332.

Wdowinski, S., O'Connell, R. J., & England, P. (1989). A continuum model of continental deformation above subduction zones: Application to the Andes and the Aegean. *Journal of Geophysical Research*, *94*(B8), 10331–10346. https://doi.org/10.1029/JB094iB08p10331.

Yue, H., & Lay, T. (2013). Source rupture models for the Mw 9.0. (2011). Tohoku earthquake from joint inversions of high-rate geodetic and seismic data. *Bulletin of the Seismological Society of America,103*(2B), 1242–1255. https://doi.org/10.1785/0120120119.